

EFFECT OF STRAIN RATE AND TEMPERATURE ON FRACTURE AND  
DAMAGE OF MAGNESIUM ALLOY AZ31B

A Thesis

by

ANA KARINA RODRIGUEZ ATENCIO

Submitted to the Office of Graduate and Professional Studies of  
Texas A&M University  
in partial fulfillment of the requirements for the degree of

MASTER OF SCIENCE

Chair of Committee,	Amine Benzerga
Co-Chair of Committee,	Ibrahim Karaman
Committee Members,	Mohammad Naraghi
	Georges Ayoub
Head of Department,	Ibrahim Karaman

May 2015

Major Subject: Materials Science and Engineering

Copyright 2015 Ana K. Rodriguez Atencio

## ABSTRACT

Due to their low density and high specific strength, magnesium and its alloys are structural metals attractive for the aerospace and automotive industries. However, wide spread use of wrought magnesium is challenged by its limited formability at low temperature compared to aluminum and steel. This results in costly production and processing of sheet and plate material. Extensive research has been carried out on deformation mechanisms, mechanical characterization, new processing routes and alloying systems in order to overcome these limitations. However, the available literature on damage and fracture is limited. In particular, the effects of temperature and strain rate on damage and fracture remain unexplored. The purpose of this study is to investigate this effects on damage accumulation to fracture in a magnesium alloy. Twin roll cast magnesium plates of AZ31B were used to that end. An extensive experimental campaign of tensile tests at various strain rates and temperatures was performed with this aim. In addition, a series of interrupted tests were carried out to investigate the microscopic damage mechanisms by means of optical and scanning electron microscopy.

The materials were found to have a positive strain rate sensitivity and showed thermal softening. Microstructural studies revealed an increased propensity to form deformation twinning at higher strain rates and lower temperatures, as expected. The fracture behavior was characterized in terms of the work to fracture ( $W_f$ ).  $W_f$  exhibited a maximum at some strain rate dependent on temperature. Conversely, at a fixed strain rate,  $W_f$  showed a maximum at a temperature dependent on strain rate. To understand

these trends, microscopy analysis was carried out on selected conditions. Under all the conditions examined, two main damage sites were identified: second phase particles and twinning. However, the propensity for twin-sized cracks was highest under conditions where the density of twinning was lowest. Different scenarios are explored in order to rationalize this behavior.

## DEDICATION

To my parents, Ali and Thais.

## ACKNOWLEDGEMENTS

Firstly, I would like to thank my committee chair and advisor. Dr. Amine Benzerga, for his guidance, motivation, support and encouragement throughout the course of this research and during the course of my master degree. Thanks for being my mentor and sharing your knowledge with me. Special thanks to Dr. Georges Ayoub for his dedication, advice and support during the last 3 years. I would also like to thank the members of the committee: Dr. Ibrahim Karaman, Dr. Mohammad Naraghi. And Dr. Jean-Briac le Graverend for their time, guidance and support.

Thanks also to Dr. Ghassan Kridli, Dr. Eyad Masad and Dr. Hassan Bazzi for inspiring me to work in research and continue my education with a master degree.

I would like to thank Ms. Jan Gerston, Ms. Karen Knabe, Ms. Michelle Newton and Ms. Hanna Prichard for their invaluable help during these two years.

Special thanks to all my classmates and friends for making my stay in College Station an enjoyable one: Kyungjun Lee (Jun), John Reeks and Luke Johnson.

Thanks to my family for their support, love and prayers. Colby, thanks for being there for me, for listening to me and encouraging me.

I would like to extend my gratitude to the Qatar National Research Foundation (QNRF) for providing economical support for this study.

## TABLE OF CONTENTS

	Page
ABSTRACT .....	ii
DEDICATION .....	iv
ACKNOWLEDGEMENTS .....	v
TABLE OF CONTENTS .....	vi
LIST OF FIGURES .....	vii
LIST OF TABLES .....	xii
CHAPTER I INTRODUCTION .....	1
CHAPTER II MECHANICAL BEHAVIOR AND MICROSTRUCTURE EVOLUTION OF TRC AZ31 MG ALLOY AT VARIOUS STRAIN RATES AND TEMPERATURES.....	11
2.1 Introduction .....	11
2.2 Experimental Method .....	13
2.3 Results and Discussion .....	15
2.4 Conclusions .....	32
CHAPTER III DAMAGE AND FRACTURE OF TRC AZ31B MAGNESIUM ALLOY AT VARIOUS STRAIN RATES AND TEMPERATURES .....	34
3.1 Introduction .....	34
3.2 Experimental Method .....	36
3.3 Results and Discussion .....	40
3.4 Conclusion.....	72
CHAPTER IV CONCLUSIONS .....	74
REFERENCES .....	77
APPENDIX .....	89
A.1 Damage on TS Planes.....	89
A.2 Twinning in post-deformed specimen .....	92
A.3 Twin sized voids.....	94

## LIST OF FIGURES

	Page
Figure 1.1 Comparison of the forming capacity of a) mild steel at room temperature, b) AZ31 at room temperature, reprinted with permission from [5]. .....	3
Figure 1.2 Scheme of the twin roll casting process, reprinted with permission from [8]. .....	5
Figure 1.3 Different slip systems in magnesium: Basal- $\langle a \rangle$ , prismatic $\langle a \rangle$ , pyramidal- $\langle a \rangle$ -pyramidal- $\langle c+a \rangle$ and twinning $\langle c+a \rangle$ , reprinted with permission from [17]. .....	6
Figure 1.4 Optical micrograph of magnesium alloy after room temperature uniaxial extrusion to a) 10% and b) 25%, showing twinning bands, reprinted with permission from [19]. .....	7
Figure 1.5 Cracked particles observed in an AZ61 magnesium alloy, reprinted with permission from [21]. .....	8
Figure 1.6 Crack along twinning interface, , reprinted with permission from [15]. .....	9
Figure 2.1 a) Geometry of the tensile sample, dimensions are in mm; b) pole figures indicating basal texture of the plates, indicating orientation of the crystalline structure according to the scheme in c). .....	15
Figure 2.2 Stress strain curves from tensile testing of TRCAZ31 at different strain rates and for temperatures equal to: a) RT and b) 300°C. ....	18
Figure 2.3 Stress strain curves from tensile testing of TRC AZ31 at different temperatures and for strain rates equal to a) $10^{-4} \text{ s}^{-1}$ , b) $10^{-3} \text{ s}^{-1}$ , c) $10^{-2} \text{ s}^{-1}$ , d) $10^{-1} \text{ s}^{-1}$ . .....	19
Figure 2.4 Yield stress vs. strain rate and calculation of the strain rate sensitivity at 100, 150, 200, 250 and 300°C. ....	21

	Page
Figure 2.5 Relation between natural logarithms of the yield stress and temperature reciprocal. ....	23
Figure 2.6 Microstructure of the fracture zone of the: a) as received alloy and specimens deformed at room temperature and strain rates of b) $10^{-1} \text{ s}^{-1}$ , c) $10^{-3} \text{ s}^{-1}$ and d) $10^{-4} \text{ s}^{-1}$ . ....	24
Figure 2.7 Microstructure of TRC AZ31B alloy of the: a) as-received and deformed at RT and strain rates of b) at $10^{-1} \text{ s}^{-1}$ , c) at $10^{-3} \text{ s}^{-1}$ , and d) at $10^{-4} \text{ s}^{-1}$ .....	25
Figure 2.8 Evolution of the microstructure during tensile deformation at $10^{-3} \text{ s}^{-1}$ and $300^\circ\text{C}$ at different deformation levels: a) 0, b) 0 + 30 min heating at $300^\circ\text{C}$ , c) 0.2, d), 0.4, and e) 0.6.....	27
Figure 2.9 Average grain size as function of the strain for tensile deformation at $10^{-3} \text{ s}^{-1}$ and $300^\circ\text{C}$ . ....	28
Figure 2.10 Evolution of the microstructure during tensile deformation at $10^{-3} \text{ s}^{-1}$ at: a) RT and; b) at $300^\circ\text{C}$ . ....	29
Figure 2.11 Evolution of the microstructure after 8 h of annealing at different treatment temperatures a) as-received, b) $100^\circ\text{C}$ , c) $300^\circ\text{C}$ , d) $375^\circ\text{C}$ , and e) $475^\circ\text{C}$ .....	30
Figure 2.12 Average grain size in function of temperature after 8 h of annealing .....	31
Figure 2.13 Evolution of the microstructure after annealing at $475^\circ\text{C}$ for the following times: a) 30 min, b) 1 h, c) 5 h, and d) 8 h.....	31
Figure 3.1 Tensile specimen geometry and reference coordinates: longitudinal (L), transversal (T), through thickness or short transversal (S). The three studied planes: TS, LT and LS.....	36
Figure 3.2 a) Initial microstructure in the LT and LS planes and b) Initial orientation of the material.....	38

	Page
Figure 3.3 Engineering stress vs strain curves of TRC AZ31B plates under tensile tests at various strain rates and: a) room temperature (RT), b) 100 and c) 300°C.....	42
Figure 3.4 Engineering stress vs strain curves of TRC Z31B plates under tensile tests at a) $10^{-1}$ , b) $10^{-3}$ and c) $10^{-4} \text{ s}^{-1}$ at various temperatures. ....	44
Figure 3.5 Strain to failure $\epsilon_f$ : a) vs strain rate, b) vs temperature. ....	46
Figure 3.6 a) Strain along the S direction $\epsilon_S$ vs strain rate and b) Strain along the T direction $\epsilon_T$ vs strain rate. ....	47
Figure 3.7 Work to fracture ( $W_f$ ) vs: (a) strain rate for various test temperatures, (b) temperature for various strain rate. Dotted circles indicate conditions selected for further studies. ....	50
Figure 3.8 Fracture surface of tensile specimen tested at various strain rates at 100°C.....	52
Figure 3.9 Fracture surface of tensile specimen tested at various strain rates and 300°C.....	53
Figure 3.10 Fracture surface of tensile specimen tested at 200°C and various strain rates. ....	55
Figure 3.11 Fracture surface of tensile specimen tested at $10^{-3} \text{ s}^{-1}$ and various temperatures. ....	56
Figure 3.12 OM micrograph of uniaxial tensile specimen interrupted at strain before failure at $10^{-3} \text{ s}^{-1}$ and $10^{-1} \text{ s}^{-1}$ : a) LS plane and b) LT plane.....	58
Figure 3.13 OM micrograph of uniaxial tensile specimen tested interrupted at strain before failure at $10^{-3} \text{ s}^{-1}$ showing: a) micro cracks propagated along twin bands, b) micro cracks parallel to the L direction, c) micro cracks perpendicular to the L direction. ....	61
Figure 3.14 EDS spectra for particles found in $10^{-3} \text{ s}^{-1}$ 100°C micro-voids. ....	62

	Page
Figure 3.15 OM micrograph of the specimen tested at $10^{-1} \text{ s}^{-1}$ and $100^\circ\text{C}$ : a) Detail from an interrupted specimen; and b) Profuse twinning, however, no micro-voids are observed along twinning bands. ....	63
Figure 3.16 EDS spectra for particles found in $10^{-1} \text{ s}^{-1}$ $100^\circ\text{C}$ micro-voids. ....	64
Figure 3.17 OM micrograph of post-mortem specimen tested at $10^{-3} \text{ s}^{-1}$ : a) Detail of coalescence of twin-related and second phase particle nucleated voids. b) Micro crack near fracture surface. ....	65
Figure 3.19 OM micrograph of uniaxial tensile specimen tested interrupted at strain before failure at $10^{-1} \text{ s}^{-1}$ and $200^\circ\text{C}$ showing: a) second-phase nucleated micro-cracks on the specimen surface and, b) micro cracks elongated along twin bands found exclusively in the mid-section of the specimen. ....	68
Figure 3.20 The dependence of volume fractions of contraction and double twins on strain rate in the AZ31, reprinted with permission from [62]. ....	72
Figure A.1.1 TS micrographs of TRC AZ31B alloy loaded at $10^{-3} \text{ s}^{-1}$ and $100^\circ\text{C}$ . ....	89
Figure A.1.2 TS micrographs of TRC AZ31B alloy loaded at $10^{-1} \text{ s}^{-1}$ and $100^\circ\text{C}$ . ....	90
Figure A.1.3 LT micrographs of TRC AZ31B alloy loaded at $10^{-3} \text{ s}^{-1}$ and $100^\circ\text{C}$ . ....	91
Figure A.1.4 LT micrographs of TRC AZ31B alloy loaded at $10^{-1} \text{ s}^{-1}$ and $100^\circ\text{C}$ . ....	91
Figure A.2.1 Twinning found on the LS plane of specimens deformed at $10^{-1} \text{ s}^{-1}$ and $100^\circ\text{C}$ . ....	92
Figure A.2.2 Twinning found on the LT plane of specimen deformed at $10^{-2} \text{ s}^{-1}$ and RT. ....	92
Figure A.2.3 Twinning found on the LT plane of specimen deformed at $10^{-3} \text{ s}^{-1}$ and RT. ....	93
Figure A.2.4 Twinning found on the LT plane of specimen deformed at $10^{-1} \text{ s}^{-1}$ and RT. ....	93

	Page
Figure A.3.1 Twin sized voids found on the LS plane of specimen deformed at $10^{-1}$ $s^{-1}$ and $200^{\circ}C$ .....	94
Figure A.3.2 Twin sized voids found on the TS plane of specimen deformed at $10^{-3}$ $s^{-1}$ and $100^{\circ}C$ .....	94
Figure A.3.3 Twin sized voids found on the LS plane of specimen deformed at $10^{-3}$ $s^{-1}$ and $100^{\circ}C$ .....	95

## LIST OF TABLES

	Page
Table 1.1 Magnesium advantages on weight reduction, reprinted with permission from [1]. .....	1
Table 2.1 Tensile test experimental plan.....	14

CHAPTER I  
INTRODUCTION

The increasing interest in magnesium alloys in the last two decades has been driven by the high specific mechanical properties of magnesium and its alloys. Being the lightest structural metal with good mechanical properties, magnesium is of special appeal for the aerospace and automotive industries. Broad use of magnesium in the transportation industry would translate into significant reduction in weight and higher fuel efficiency.

**Table 1.1** Magnesium advantages on weight reduction, reprinted with permission from [1].

	Component							
	Engine block		Gear box + clutch housing (Al alloy)	Oil pan (Al alloy)	Four wheels		Engine cradle	
	Cast iron	Al alloy			Stee l	Al alloy	Stee l	Al alloy
Traditional solution (kg)	32	23.5	21.5+5	3	36	23	25	17.5
Magnesium alloy solution (kg)	19	15+3	2	18	18	15	15	
Weight reduction (kg)	13	4.5	6.5	1	18	5	10	2.5
Weight reduction (%)	40	19	30	33	50	22.5	40	30

Table 1.1 [1] exemplifies the potential weight reduction obtained by replacing steel or aluminum by magnesium alloys. Up to 48kg can be saved when steel and iron is replaced, and 19.5kg if aluminum is replaced. If replacing steel, this would be equivalent to savings of 0.25 liters of gasoline per 100km, and 0.1 liters per 100km in the case of aluminum.

Several studies have estimated the potential CO<sub>2</sub> emissions reduction achieved by substituting magnesium in different heavy components of cars [1-3]. These studies conclude that, if well the energy and CO<sub>2</sub> required to produce a magnesium ingot is high relative to other lightweight materials, the reduction in CO<sub>2</sub> and energy consumption as a result of weight reduction in cars overrides this higher initial cost.

However, one of the main obstacles for the replacement of aluminum and steel by magnesium is the production of wrought magnesium. While cast products are common, wrought magnesium processing and properties represent a challenge that has hindered the wide use of magnesium in some components (e.g., car door panels, sheet frames, steering, among others[2]). By 2012, only 0.3% of a typical American sedan was made of magnesium, fabricated mostly by high-pressure die casting [4]. One of the main limitations of wrought magnesium is its poor formability at low temperatures. Currently, cold-stamping is the main shaping process used for body panels parts in the automotive industry. This process, however, is not applicable to magnesium [3], as can be illustrated in figure 1.1.

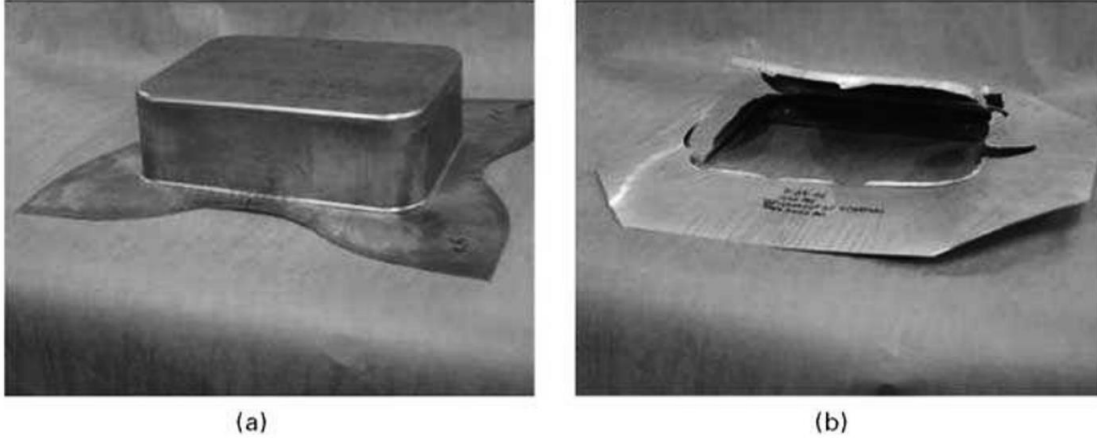


**Figure 1.1** Comparison of the forming capacity of a) mild steel at room temperature, b) AZ31 at room temperature, reprinted with permission from [5].

Therefore, the development of wrought magnesium is essential for application in the automobile and aerospace industries. Traditionally, the fabrication of magnesium plates and sheets consist in: i) fabrication of an ingot through direct chill casting (DC); ii) scalping of the rectangular ingots produced (of thickness around 400– 500 mm); iii) homogenizing; iv) hot rolling and v) annealing[6]. However, fabrication of magnesium plates is difficult and expensive, since several number of rolling passes and heat treatments are needed in order to overcome the limited deformation possible in each rolling step. Twin Roll Casting (TRC) emerged as an alternative method for plate production that decreases rolling and heat treatment steps. This is achieved in TRC by combining solidification and rolling in a single step, as illustrated in figure 1.2. At present, only two companies around the world, POSCO (South Korea) and Thyssen Krupp (Germany) produce TRC magnesium plates [6]. Twin roll casting (TRC) is

considered the most efficient fabrication technique for magnesium plates and sheet currently commercially available.

Despite TRC being used for aluminum, copper and steel for some time, TRC of magnesium still faces some challenges due to high oxidation reactivity and low specific heat. More importantly, despite the potential cost reduction provided by TRC, the products obtained by this technique have similar issues to those of wrought products obtained by more traditional processes. Such issues are strong basal texture and poor room temperature deformation.

The poor formability of wrought magnesium at low temperatures is commonly associated to its propensity to develop a basal texture and to the anisotropic nature of its high  $c/a$  ratio HCP structure. The basal texture is developed during processes such as extrusion or rolling, which promotes the alignment of the  $\{0001\}$  basal planes with the rolling or extrusion direction. Different processes such as equal channel angular plate extrusion (ECAPE) have been developed in order to reduce the basal texture of wrought magnesium and for grain refinement [7], however, such processes are not yet applied at an industrial level.

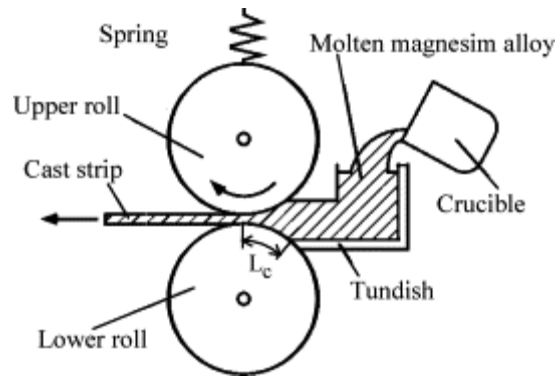


**Figure 1.2** Scheme of the twin roll casting process, reprinted with permission from [8].

The basal texture is accompanied by the anisotropic plastic response of the HCP structure of magnesium. Basal, prismatic and pyramidal slip systems with type  $\langle a \rangle$  Burgers vectors are available in magnesium (schematized in figure 1.3). Together, they provide magnesium with only 4 independent slip systems [9]. However, for homogenous deformation of a polycrystalline material, 5 independent slip systems should be active in order to satisfy Taylor and von Mises criteria. Strain along the  $\langle a \rangle$  direction is readily accommodated by the aforementioned slip systems, while compression or tension along the  $\langle c \rangle$  axis cannot be supported by any dislocation with type  $\langle a \rangle$  Burgers vector. The occurrence of non-basal slip such as prismatic slip of  $\langle a \rangle$  type Burgers vector and pyramidal  $\langle c+a \rangle$  slips has been controversial, since early single crystal works on magnesium did not reveal the activity of these mechanisms [9]; but it has been proven on more recent works [10, 11]. Several studies have reported plasticity at room temperature, which can be attributed to the activity of non-basal slip and deformation twinning [10, 12]. Nonetheless, the critical resolved shear stress (CRSS) for non-basal slip modes in magnesium are much higher than those of basal slip [13] and thus basal slip and

twinning are believed to dominate during deformation. Twinning arises as an additional mechanism to accommodate deformation along the  $\langle c \rangle$  axis (figure 1.4). Different types of twinning can be active in the following planes of a HCP material:  $\{10\text{-}12\}$ ,  $\{30\text{-}34\}$ ,  $\{10\text{-}13\}$ ,  $\{11\text{-}24\}$ ,  $\{10\text{-}11\}$  and  $\{10\text{-}14\}$ . For magnesium, however, some twins are more readily formed and observed, depending on the type of strain imposed on the  $c$ -axis [14]. These twins are classified in extension and contraction twinning. The extension twin forms as the crystal tries to accommodate the extension of the  $c$ -axis, and corresponds to the  $\{10\text{-}12\}$  plane [12]. Contraction twinning accommodates the compression of the  $c$ -axis which often involves a double twinning mechanism: the primary twinning forms on the  $\{10\text{-}11\}$  or  $\{10\text{-}13\}$  planes, which are the contraction twins, followed by a secondary twin in the  $\{10\text{-}12\}$  plane, which correspond to an extension twin. The double twinning results in a reorientation of the crystal of about  $38^\circ$ , an alignment that favors basal slip [14-16].

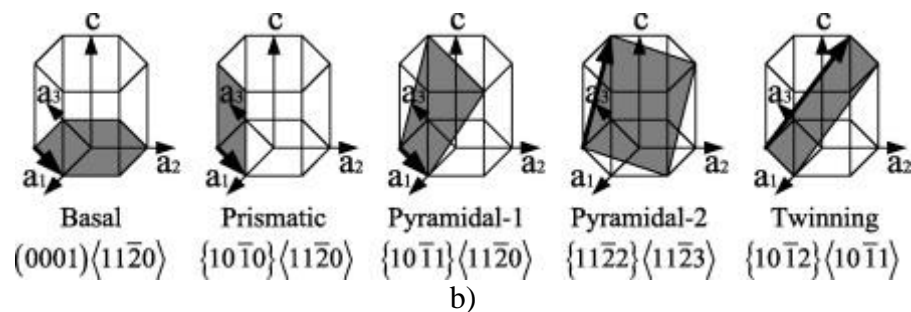


**Figure 1.3** Different slip systems in magnesium: Basal- $\langle a \rangle$ , prismatic  $\langle a \rangle$ , pyramidal- $\langle a \rangle$ -pyramidal-  $\langle c+a \rangle$  and twinning  $\langle c+a \rangle$ , reprinted with permission from [17].

While deformation mechanisms in magnesium have been studied in depth, fracture and damage have been overlooked. The plastic anisotropy plays an important part when studying the fracture and damage of wrought magnesium. The surface energy of non-basal planes is higher than that of the basal plane for HCP materials, thus, the orientation of the crack with respect to the crystallographic orientation of the material will be crucial on the fracture toughness. Recent studies [18] found that for magnesium AZ31, the ductility is higher at moderate levels of triaxiality. This suggests that under triaxial loading more deformation mechanisms become active in magnesium.

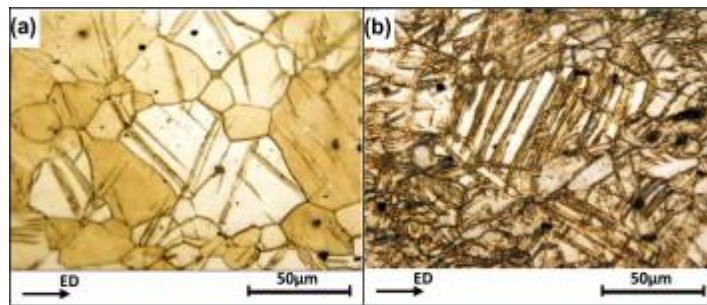


**Figure 1.4** Optical micrograph of magnesium alloy after room temperature uniaxial extrusion to a) 10% and b) 25%, showing twinning bands, reprinted with permission from [19].

The available studies in damage of magnesium have identified mainly two sources damage or nucleation sites: second phase particles and twins. Similar to aluminum and steels, second phase particles are active in the damage initiation of magnesium alloys (figure 1.5). In AZ (aluminum-zinc) systems, three different types of inclusions are formed: oxide/intermetallics, Mn-Al and Mg-Al inclusions; being the

$Mg_{17}Al_{12}$   $\beta$ -phase the most commonly identified precipitate [20-24], identification often based on a ternary phase diagrams. However, the AZ31 system is more than a ternary system, since commercial alloys contain additions such as Mn to enhance corrosion resistance [22] and traces of Si can also be found. Therefore, in the solid state, AZ31 can form different Mn-Al intermetallics such as  $MnAl_{14}$ ,  $MnAl_{16}$  [21],  $Al_8Mn_5$  [20]. These Mn-Al particles, together with MgSi intermetallics [25] have been identified in the literature as initiation sites for cracks and micro-voids formation [21, 24, 25].

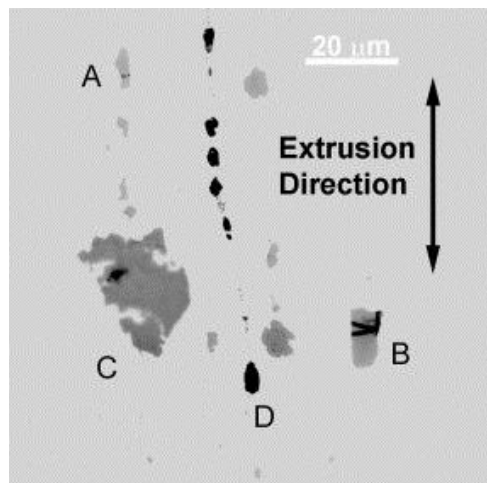


**Figure 1.5** Cracked particles observed in an AZ61 magnesium alloy, reprinted with permission from [21].

In addition to precipitates and inclusions, another important source of damage in magnesium is twinning (figure 1.6). Indeed, the importance of twinning in damage initiation in magnesium is illustrated by the following fact: pure magnesium does not exhibit an enhanced ductility compared to its alloys, unlike the case of pure aluminum.

Evidence of twinning as nucleation site for micro-voids has been reported by some studies [13, 15, 18, 26-28]. With some variance [29, 30], {10-11}–{10-12} double twin has been associated with crack formation in magnesium alloys[31]. Some studies suggest a complex relationship between twinning and damage initiation. It has been proposed [32] a cyclic process in which a crack is created, high stress concentration in the crack edges promote twinning, and these twinning in turn promote more cracks.

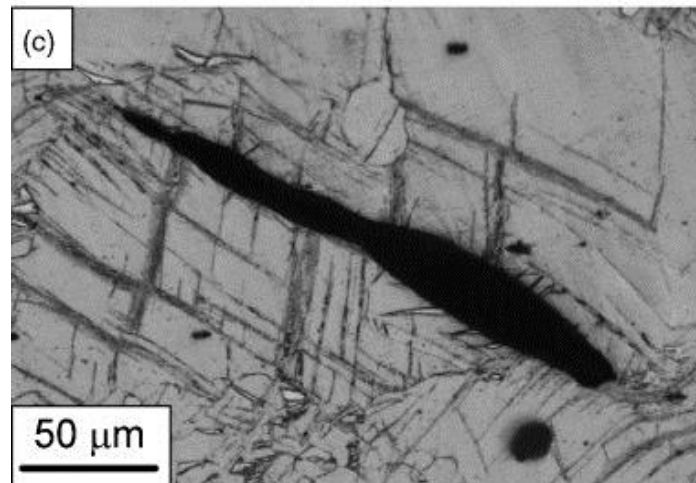


**Figure 1.6** Crack along twinning interface, , reprinted with permission from [15].

In addition to the limited number of studies on fracture and damage in magnesium alloys, most of the existing work focuses on the behavior at a single temperature or single strain rate. To address this gap, an extensive experimental campaign with the aim of offer a better understanding of the influence of strain rate and temperature on the fracture and damage process of magnesium was carried out. This

would benefit the design of new magnesium alloying systems and forming processes and the prediction capabilities of current material models

The two major goals of this study can be summarized as:

- i) Characterize the tensile mechanical behavior and microstructure of twin roll casted TRC AZ31B magnesium alloys under a wide range of strain rates and temperatures.
- ii) Investigate the influence of strain rate and temperature on damage and fracture on magnesium alloys.

The work presented in this thesis has been grouped in two main chapters, each of them corresponding to an original research paper that has resulted from this study: chapter II corresponds to a paper published in the Journal of Materials Engineering and Performance (JMEP), while chapter III corresponds to a paper ready to submission to Materials Science and Engineering A (MSEA). Additional results, not included in these chapters for brevity reasons, have been annexed in the Appendix section.

## CHAPTER II

### MECHANICAL BEHAVIOR AND MICROSTRUCTURE EVOLUTION OF TRC AZ31 MG ALLOY AT VARIOUS STRAIN RATES AND TEMPERATURES\*

#### 2.1 Introduction

In recent years, the demand for lightweight materials with good mechanical properties has increased. For the automobile industry, weight reduction translates into decreased fuel consumption with a positive environmental impact (saving natural energy resources and reducing CO<sub>2</sub> emissions). In this context, magnesium alloys have a major potential since magnesium is the lightest structural metal and possesses high specific strength [33] excellent thermal conductivity, damping, electromagnetic shielding, and recycling properties [34, 35]. However, the hexagonal-closed pack (HCP) crystal structure of magnesium provides only four independent slip systems, less than the five slip systems required to accommodate plastic deformation. This limits the formability at low temperatures, making the manufacturing of wrought material expensive [36-38].

One method to produce magnesium sheets is through the twin-rolled casting (TRC) process. The TRC process is performed by feeding molten metal into a gap between two water-cooled rolls, achieving a continuous sheet production [39, 40]. Compared with the hot-rolling manufacturing of magnesium sheets; TRC reduces the

---

\* Reprinted with permission from “Effect of the strain rate and temperature on the microstructure evolution of twin roll cast wrought AZ31B alloys sheet.” by A.K. Rodriguez, G. Ayoub, G. Kridli, H. Zbib, 2013. *Journal of Materials Engineering and Performance*, 22, 3115-3125, Copyright 2013 by Springer.

number of rolling passes, decreases the temperature, and offers materials with finer microstructure [41-45]. However, a massive use of the magnesium TRC sheets is not yet viable since this final product still faces formability limitations in downstream processes [36, 41]. For these reasons, a good understanding of the behavior of the industrially obtained magnesium sheets is important to achieve improved formability through adequate processing conditions. The present study explores the effects of temperature and strain rate on the deformation behavior and the evolution of microstructure of AZ31B as-rolled, twin-rolled cast sheets. Several studies on the processing methods and properties of TRC AZ31 magnesium alloys are reported in the literature. These included study of the effect of the addition of refiners [46] ; the microstructure of the as-cast TRC plates [47] and [41]; the mechanical behavior of annealed TRC [33]; the microstructural evolution of annealed TRC AZ31B [45], the effect of the initial texture on the anisotropy of AZ31. [48]; among others.

In this study, we present the results of a systematic investigation of the effects of thermomechanical variables on the deformation behavior and on the microstructure of the commercially available as-rolled TRC AZ31B sheets. The study aims at providing a better insight on the behavior of the material to facilitate future application in the industry.

## 2.2 Experimental Method

### *Material*

The material investigated was twin-rolled cast AZ31B sheets, rolled to a final thickness of 3 mm and supplied by POSCO. The chemical composition of the material was obtained through energy dispersive x-ray analysis. The results presented in wt.% are as follows: Mg 95.4%, Al 3.32%, Zn 0.803%, Mn 0.304%, and Si 0.147%. The initial microstructure shown in figure 2.6 had an average grain size of  $8.2 \pm 0.5 \mu\text{m}$ .

### *Tensile tests*

Tensile tests were performed under temperatures between room temperature (RT) and  $300^\circ\text{C}$  and at strain rates from  $10^{-4}$  to  $10^{-1} \text{ s}^{-1}$ , as shown in Table 2.1. The test specimens were machined from the supplied AZ31B sheets according to the shape and size presented in figure 2.1. The geometry features of the sample were chosen according to the description given by [49, 50] and ASTM E2448-11. The major axis of each specimen was aligned parallel to the rolling direction, and thus, the tensile load was parallel to the rolling direction of the material. While the highest tensile testing temperature in this investigation was  $300^\circ\text{C}$ , the selection of the specimen geometry according to ASTM E2448-11 was mainly because of the author's interest in using the same specimen size in a future study on the superplastic flow behavior of AZ31B. It is worth mentioning that all of the tested specimens in this present study failed in the middle region (away from the shoulders) of the gage section.

**Table 2.1** Tensile test experimental plan

Temperature [°C]	Strain rate [s <sup>-1</sup> ]						
	0.0001	0.0005	0.001	0.005	0.01	0.05	0.1
RT	✓	✓	✓	✓	✓	✓	✓
100	✓		✓		✓		✓
150	✓		✓		✓		✓
200	✓		✓		✓		✓
250	✓		✓		✓		✓
300	✓	✓	✓	✓	✓	✓	✓

The tensile tests were conducted using an electromechanical screw-driven testing machine (MTS Insight 30 kN) equipped with a ThermoCraft environmental chamber. In order to achieve a homogenous heat up, all the samples were loaded into the test fixture and then preheated for 30 min at the desired test temperature before the test.

#### *Microstructural studies*

The microstructural evolution was investigated under various strain rates, temperatures and strain levels; the latter achieved through interrupted tensile tests. The microstructures were observed through a Carl Zeiss optical microscope. The specimens were prepared by mechanical grinding and polishing. The polished specimens were then etched using an acetic-picral solution, with a 5:2 acetic-to-picric acid ratio. Finally, the observed grains in the revealed microstructure were measured using the ASTM E1382 automatic method incorporated in the AxioVision Grain Module software.

In order to investigate the effect of annealing on the microstructure, samples of 1cm<sup>2</sup> were cut and heat treated in a ThermoScientific box furnace. The annealing was

performed at four different temperatures 100, 300, 375, and 475°C with five exposition periods 15, 30, 60, 300, and 480 min.

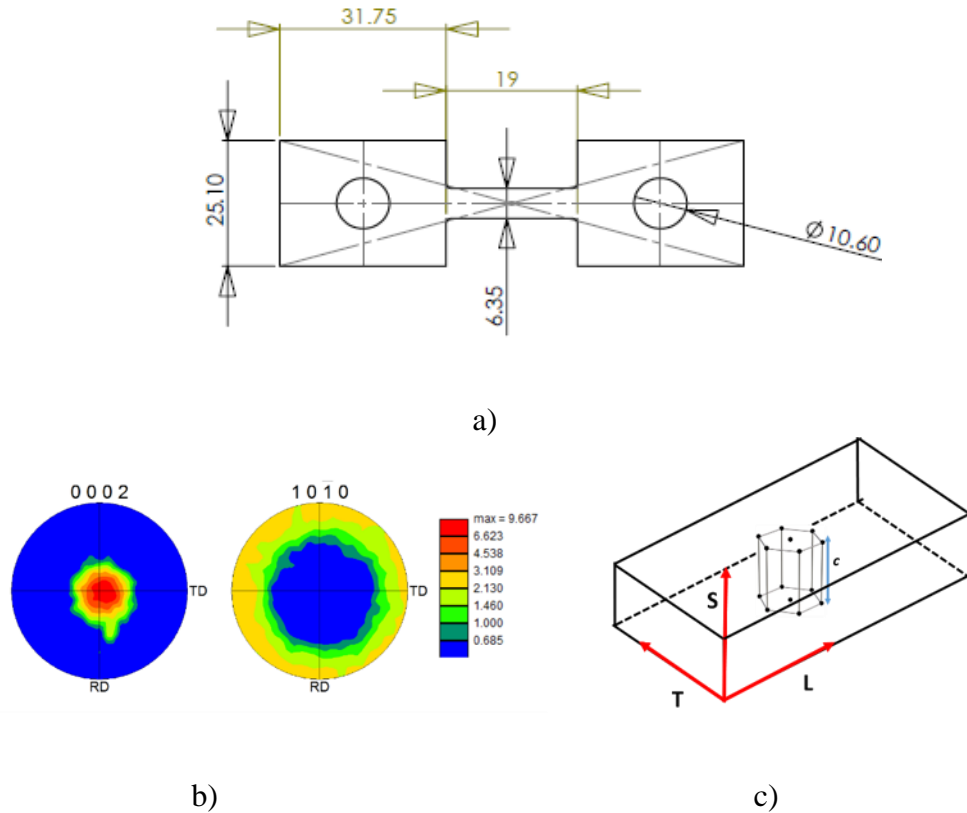


**Figure 2.1** a) Geometry of the tensile sample, dimensions are in mm; b) pole figures indicating basal texture of the plates, indicating orientation of the crystalline structure according to the scheme in c).

## 2.3 Results and Discussion

### *Tensile tests*

The mechanical behaviors of the AZ31B at the RT and at 300°C for different strain rates are shown in figure 2.2 a) and b), respectively. At the RT, the AZ31B sheet shows a semi-ductile fracture under tension. Figure 2.2 a) shows that at the RT, the strength of the AZ31B is not affected by the strain rate; however, the strain rate seems to

only affect the strain at failure. More specifically, the yield strength and the maximum stress seem to be independent of the strain rate in the studied strain rate range, with an average yield strength  $\sigma_y$  of  $220\pm 10$  MPa and an average maximum stress equal to  $270\pm 2$  MPa. It can be also pointed out that the maximum elongation to fracture was obtained at the lowest investigated strain rate of  $10^{-4} \text{ s}^{-1}$ , while the minimum elongation was obtained at the highest investigated strain rate of  $10^{-1} \text{ s}^{-1}$ . At low temperatures, the high stress and low strain exhibited by the as-rolled material are due to the limited deformation systems of magnesium. Owing to its HCP crystal structure, magnesium deforms at the RT with only three independent slipping systems, far from the five systems needed according to Von Misses criterion for a uniform plastic deformation [51, 52]. To understand the deformation mechanisms involved at RT, the orientation of the crystals in the plates needs to be taken into account. Due to their fabrication process, the plates studied are have a basal texture, i.e., the  $\{0002\}$  plane is aligned with the normal direction of the plates, as confirmed by the pole figures obtained for the as-received material and shown in figure 2.1. Hence the c axis of the crystals is mostly perpendicular to the loading direction as schematized in figure 2.2. With such configuration, prismatic slips are suppressed. And, even though pyramidal slips may occur in this setup, the CRSS for pyramidal  $\langle c+a \rangle$  slips is high at RT. Twinning has a lower CRSS than pyramidal slips [53], and so its assumed to play a major role in the deformation of magnesium at RT. The effect of the strain rate at  $300^\circ\text{C}$  is shown in the figure 2.2 b). It can be clearly observed that the behavior of the AZ31B is highly time dependent. The yield stress decreases from 104.0 MPa for a strain rate of  $10^{-1} \text{ s}^{-1}$ , to 38.8 MPa for a

strain rate of  $10^{-4} \text{ s}^{-1}$ . For these conditions, the maximum stress also decreases from 132.6 MPa ( $10^{-1} \text{ s}^{-1}$ ) to 43.8 MPa ( $10^{-4} \text{ s}^{-1}$ ). Figure 2.2b) also shows that the material ductility increases with the increasing temperature and the decreasing strain rate. In fact, an increase of 78% in elongation to fracture and a decrease of 79% in the maximum stress were obtained by decreasing the strain rate from  $10^{-1}$  to  $10^{-4} \text{ s}^{-1}$ . At lower strain rates, the strain hardening is dramatically diminished, and a more plastic deformation appears at  $10^{-4} \text{ s}^{-1}$ . These results are in agreement with the fact that, at high temperature, both pyramidal and prismatic slips are activated. The results may also indicate the activity of other high-temperature deformation mechanisms, for instance, GBS and DRX [54]. Such improvements in the availability of deformation mechanisms for AZ31B results in a pronounced strain rate effect. A deeper insight on the deformation mechanism operating during tensile deformation will be discussed together with the microstructural evolution analysis.

Figure 2.3 shows the stress-strain response of the material for a given strain rate at different temperatures. It clearly demonstrates that higher temperatures result in a decrease of the maximum stress and increase of the elongation to fracture of the material, due to the activation of a higher number of deformation systems as mentioned earlier. Figure 2.3 also shows that the effect of strain rate is more significant at higher temperatures. Furthermore, it could be noticed that the effects of the temperature and the strain rate are not independent. A better insight on the interdependency of the strain rate and temperature can be obtained by calculating and analyzing the strain rate sensitivity of the material.

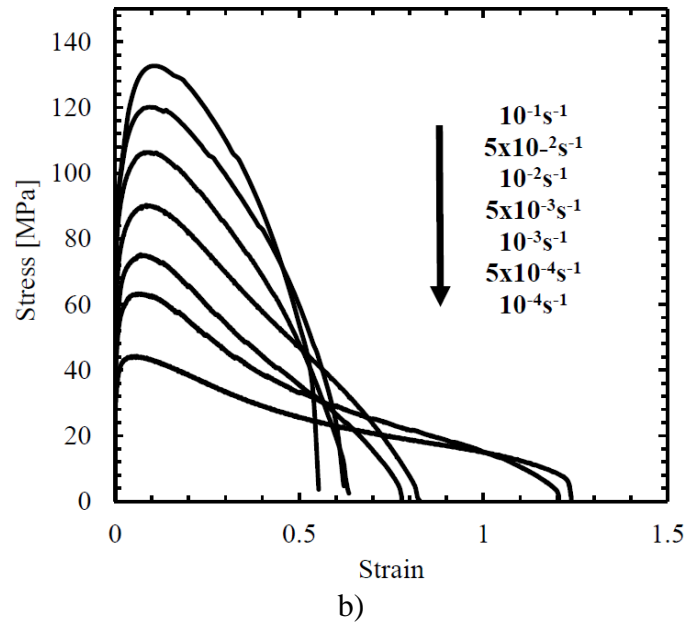
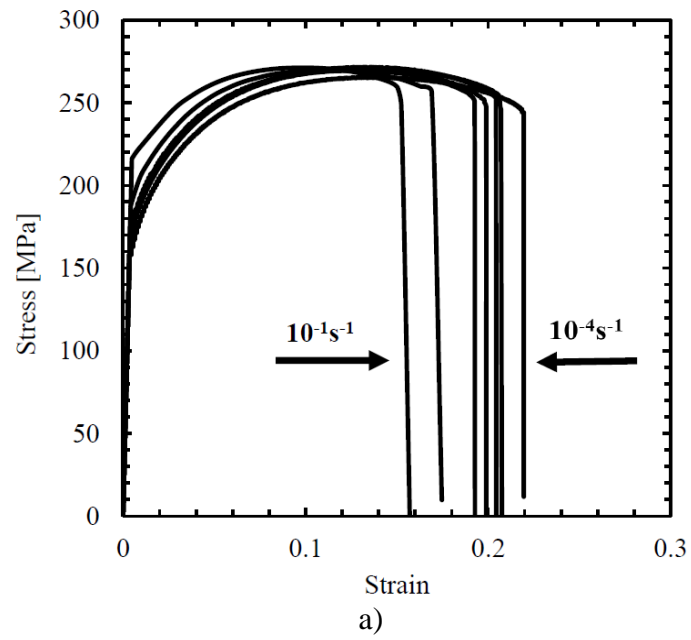


**Figure 2.2** Stress strain curves from tensile testing of TRCAZ31 at different strain rates and for temperatures equal to: a) RT and b) 300°C.

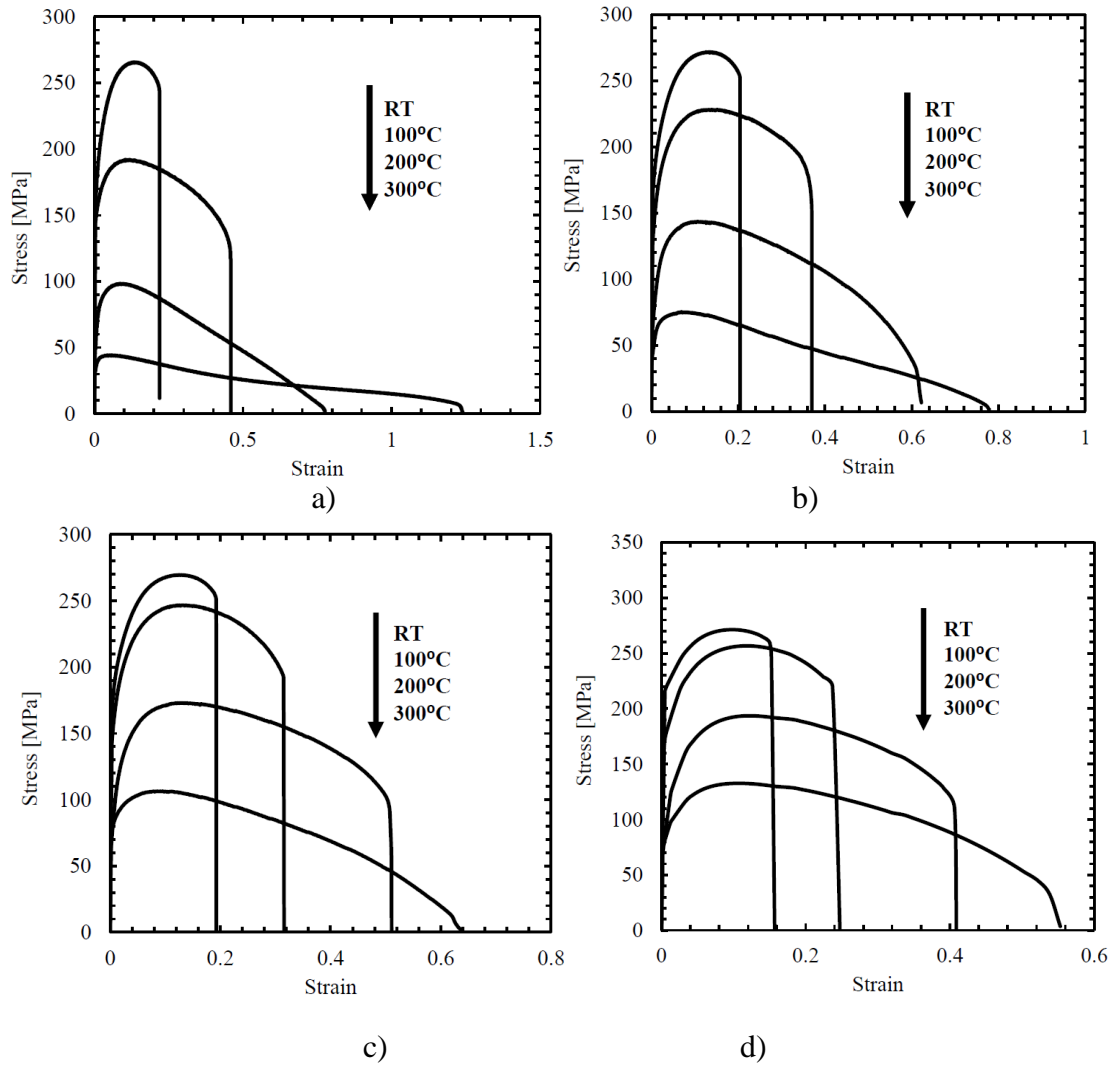


**Figure 2.3** Stress strain curves from tensile testing of TRC AZ31 at different temperatures and for strain rates equal to a)  $10^{-4} \text{ s}^{-1}$ , b)  $10^{-3} \text{ s}^{-1}$ , c)  $10^{-2} \text{ s}^{-1}$ , d)  $10^{-1} \text{ s}^{-1}$ .

### *Strain rate sensitivity*

A better understanding of the effects of the strain rate and temperature can be achieved by calculating the strain rate sensitivity factor,  $m$ , given in equation 2.2. The strain rate sensitivity factor is a parameter that indicates the effect of the strain rate on the strength of the material and represents the ability of the material to resist plastic

instability [55]. High strain rate sensitivity indicates an increase in the amount of plastic deformation with a decrease in strain rate. The strain rate sensitivity depends on temperature, microstructure, and strain rate. Figure 2.4 shows the yield stress as a function of the strain rate for a given temperature. The strain rate sensitivity is calculated by fitting experimental results to the relationship between strength, strain rate, and temperature [56] given in equation 2.1:

$$\dot{\epsilon} = A\sigma^n \exp\left(\frac{-Q}{RT}\right) \quad (2.1)$$

where  $\dot{\epsilon}$  is the strain rate, A is a material constant,  $\sigma$  is the stress at a fixed strain, n is the hardening index that is linked to the strain rate sensitivity as follows:  $n = m^{-1}$ , Q is the activation energy, R is the universal gas constant and T is the absolute temperature. This equation can be further simplified to express the relation of stress and strain rate as

$$\sigma = B\dot{\epsilon}^m \quad (2.2)$$

with  $B = A^{-m} \exp(mQ/RT)$ . The value of m is obtained by plotting  $\ln(\sigma_y)$  as a function of  $\ln(\dot{\epsilon})$  and calculating the slope of the resulting curve for a given temperature. It was observed that the strain rate sensitivity of AZ31B increases with temperature, reaching a value of  $m = 0.14$  at 300 °C. Such value is in agreement with the observed mechanical behavior, with the material being more sensitive to the strain rate at higher temperatures.

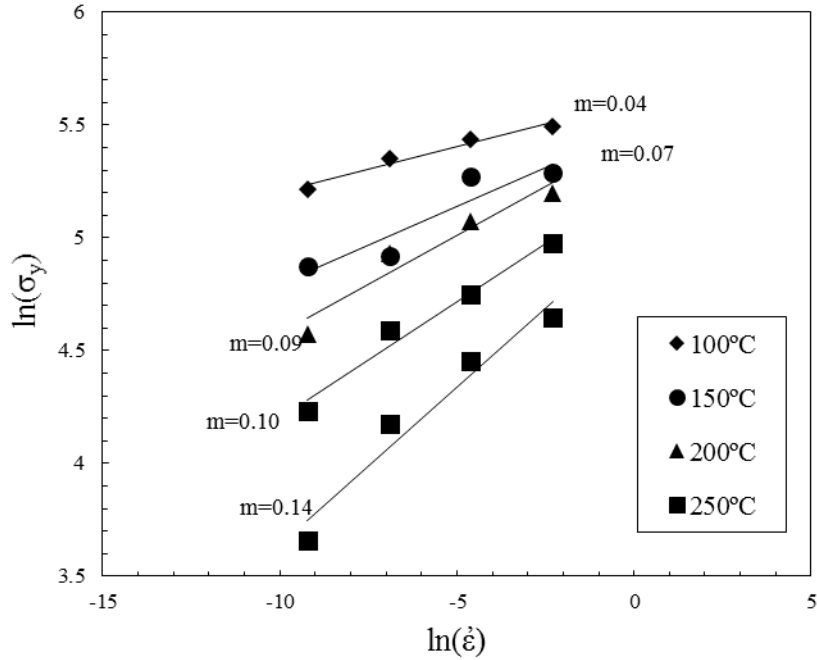


**Figure 2.4** Yield stress vs. strain rate and calculation of the strain rate sensitivity at 100, 150, 200, 250 and 300°C.

### Activation energy

The activation energy provides an insight on the processes that control the rate at which the different deformation mechanisms operate. In this study, the activation energy is calculated from equation 2.3:

$$Q = nr \left( \frac{\delta \ln(\sigma_y)}{\delta T^{-1}} \right) \text{ for a constant } \dot{\epsilon} \quad (2.3)$$

In figure 2.5,  $\ln(\sigma_y)$  is plotted as a function of  $1/T$  at various strain rates. The activation energy  $Q$  is calculated by multiplying the slope of the linear segments by  $R$  and the average value of  $n$  obtained previously, for a constant strain rate. Two different slopes can be observed in the data presented in figure 2.5, indicating two levels of

activation energy over the studied temperature range. An increase in the temperature leads to an increase of the activation energy, which is typical of HCP metals such as cadmium, zinc, and zirconium [57]. A variation on the activation energy with strain rate is also observed: at lower strain rates, higher activation energies are noticed. The average values of the activation energy in function of the temperatures are given in figure 2.5. At temperatures between 100 and 200°C, the average activation energy is 108 kJ/mol, while at temperatures between 200 and 300°C, the average activation energy is 148.6 kJ/mol. For the temperature range of 100-200°C,  $Q$  might correspond to the grain boundary diffusion activation energy ( $Q_{gb} = 92$  kJ/mol) [57]. Hence, at such temperatures, the rate-controlling mechanism could be grain boundary diffusion. Between 200 and 300°C, the activation energy might correspond to the lattice self-diffusion ( $Q_L = 135$  kJ/mol) or aluminum diffusion ( $Q_d = 145$  kJ/mol) energies, indicating that these could be the rate-controlling mechanisms at high temperature [58].

#### *Evolution of the microstructure under plastic deformation*

In this section, two different studies of the evolution of the microstructure have been conducted: i) analysis of the fractured specimens at various strain rates and temperatures, ii) analysis of the central part of the specimen at various strains at a fixed strain rate and temperature. The microstructural observations were made in the LT plane of the specimens.

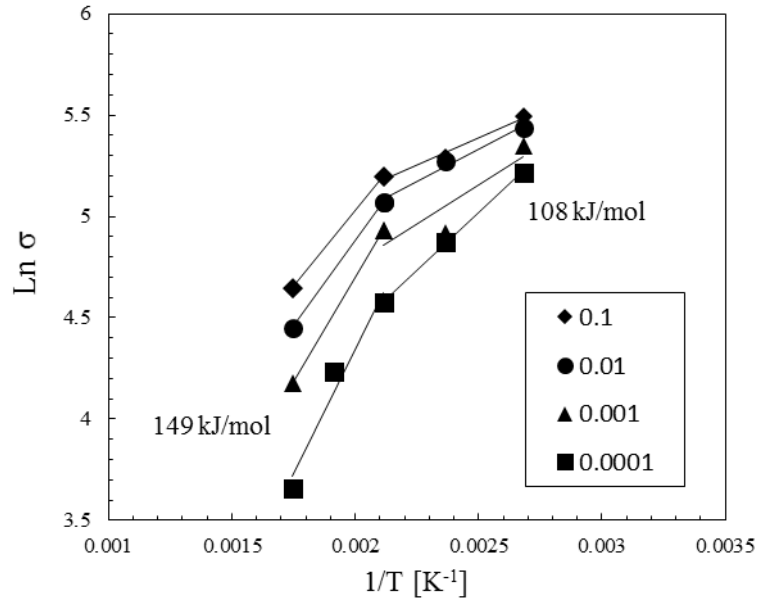


**Figure 2.5** Relation between natural logarithms of the yield stress and temperature reciprocal.

The fractured specimens at various strain rate and temperature were analyzed by taking micrographs near the fracture surfaces of test specimens. Figure 2.6 shows the microstructure of specimens tested at RT and various strain rates. As a general observation, the grain size of the material decreases after deformation, as expected. The micrographs at different strain rates show bands that we attribute to twinning, with a higher density of twinning at the highest strain rate of  $10^{-1} \text{ s}^{-1}$ . According to the literature, the basal texture of the as-rolled sheets favors contraction twinning occurring on the  $\{10\cdot11\}$  and  $\{10\cdot13\}$  twin planes [15, 59]. In turn, the texture reorientation due to twinning favors twinning at the  $\{10\cdot12\}$  plane, and thus double twinning could also be taking place [15, 59, 60].

Figure 2.7 shows the progression of the microstructure of fractured specimens for different strain rates at 300°C. It can be observed that the bands previously attributed to twinning are not present, this might indicate that twinning is not the dominating mechanism at high temperatures. It can be also observed that the grain size decreases with a decrease of the strain rate until  $10^{-3} \text{ s}^{-1}$ , reaching a minimum value of  $3.7 \pm 0.2 \text{ }\mu\text{m}$ , after which, an increased grain size is obtained with decreasing strain rate; i.e., largest grains were observed at a strain rate  $10^{-4} \text{ s}^{-1}$  compared to those observed at  $10^{-3} \text{ s}^{-1}$ . At  $10^{-4} \text{ s}^{-1}$ , the average grain size increases to  $5.1 \pm 0.3 \text{ }\mu\text{m}$ . This can be attributed to GBS since the combination of high temperature and low strain rate favors GBS.

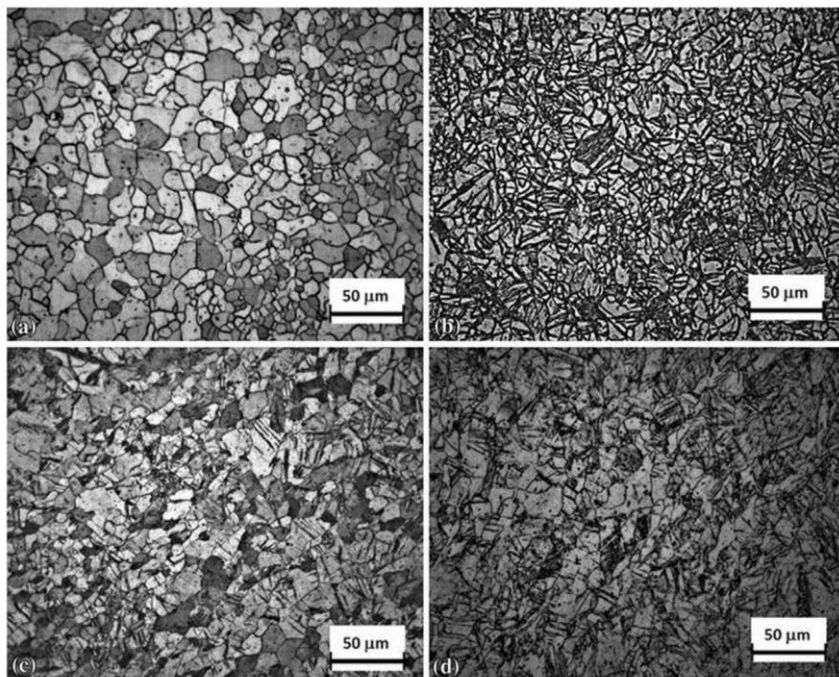


**Figure 2.6** Microstructure of the fracture zone of the: a) as received alloy and specimens deformed at room temperature and strain rates of b)  $10^{-1} \text{ s}^{-1}$ , c)  $10^{-3} \text{ s}^{-1}$  and d)  $10^{-4} \text{ s}^{-1}$ .

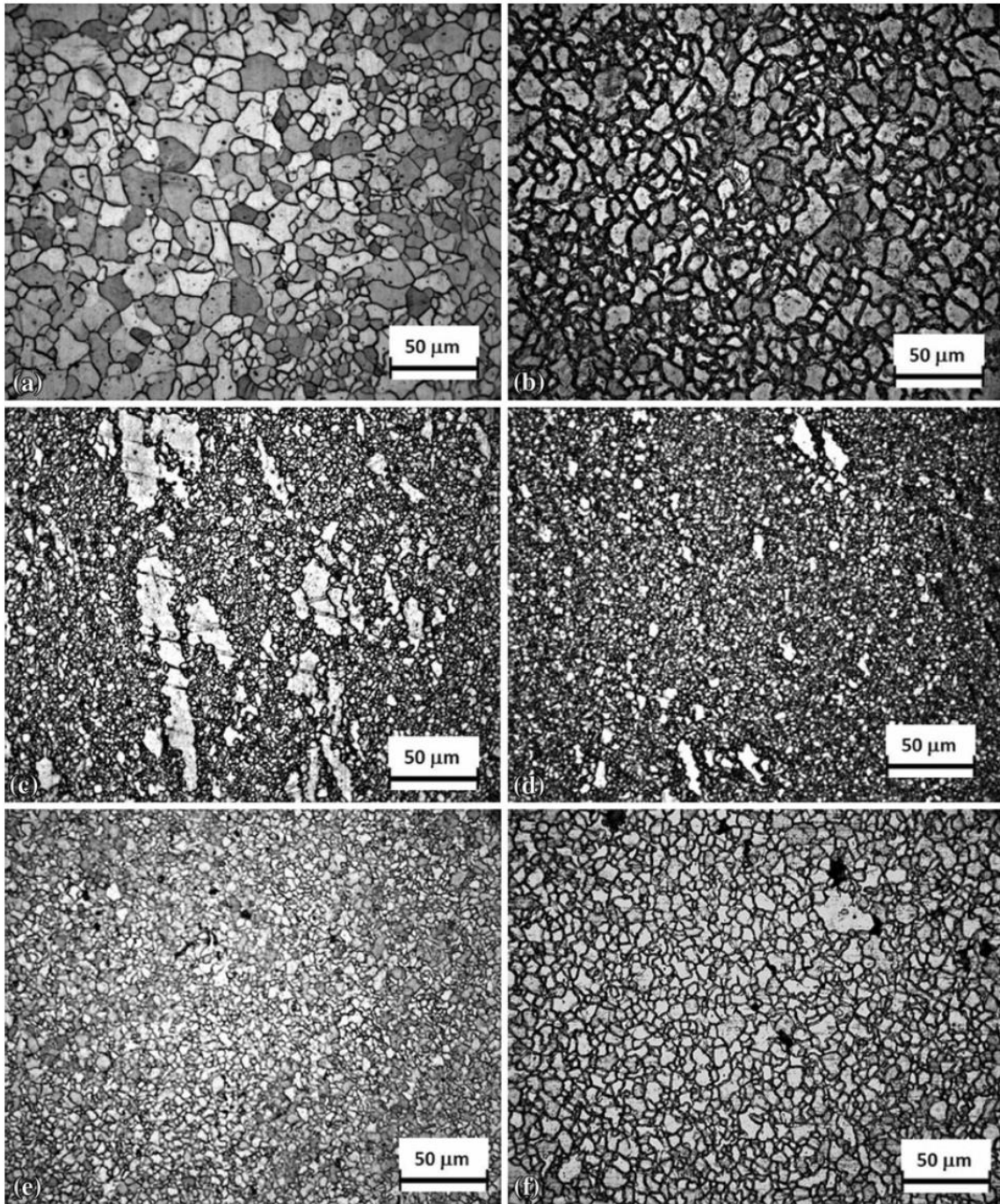
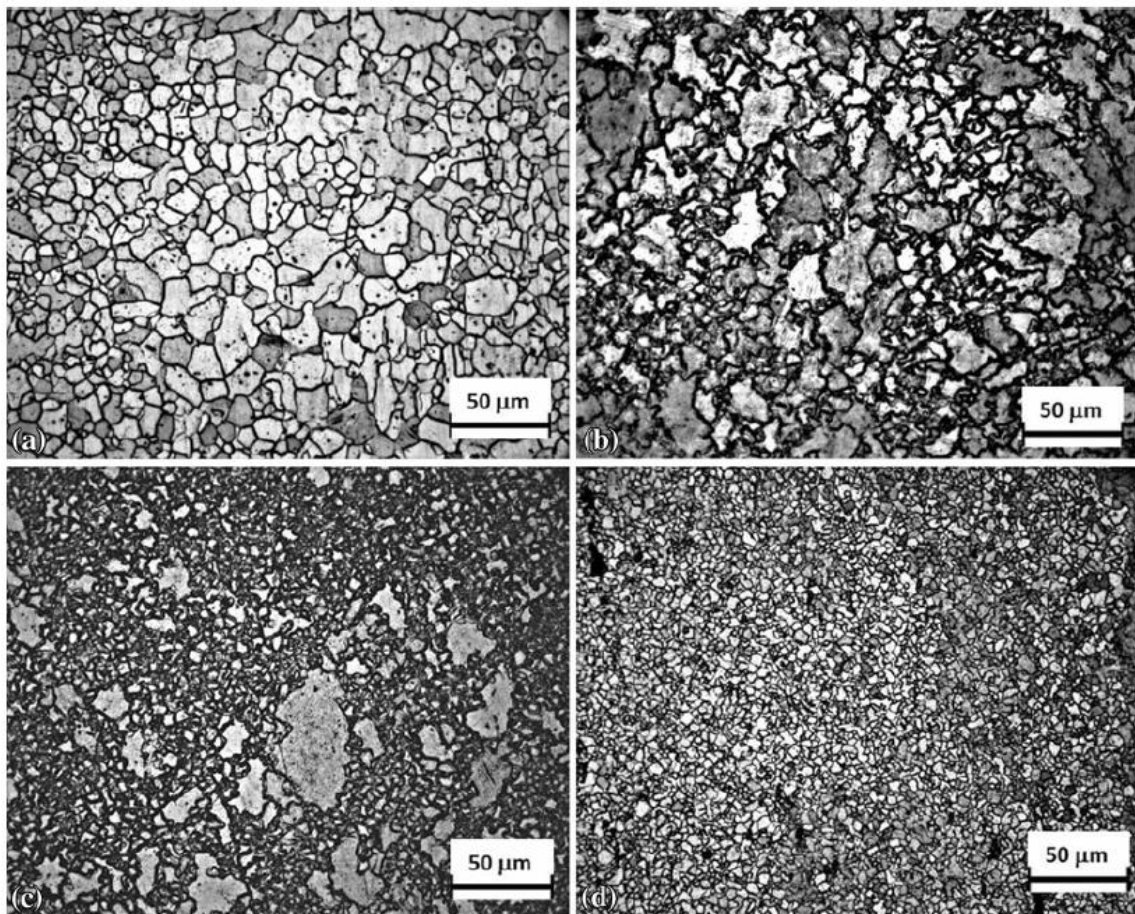


**Figure 2.7** Microstructure of TRC AZ31B alloy of the: a) as-received and deformed at RT and strain rates of b) at  $10^{-1} \text{ s}^{-1}$ , c) at  $10^{-3} \text{ s}^{-1}$ , and d) at  $10^{-4} \text{ s}^{-1}$

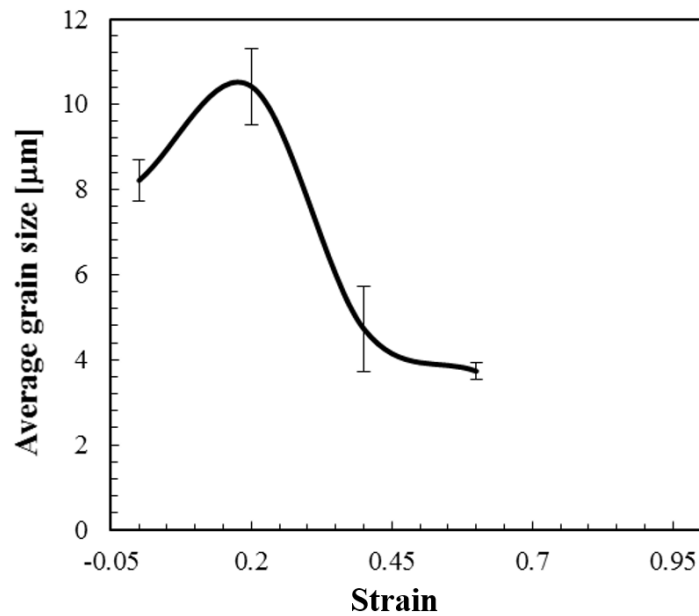
The micrographs in figure 2.7 show that, for the strain rate range  $10^{-2}$  to  $10^{-3} \text{ s}^{-1}$ , an elongation of some grains is present along the testing direction. However, when the strain rate is further decreased to  $10^{-3} \text{ s}^{-1}$  all the grains appear to be equiaxed. At  $10^{-4} \text{ s}^{-1}$  strain rate, the material exhibits a larger number of more developed voids compared to the microstructure obtained at higher strain rates. This last observation is in agreement with the stress-strain behavior shown in figure 2.2b), which shows a more ductile behavior of the material at lower strain rates. The aforementioned changes in grain size seem to correspond to DRX, which is characterized by nucleation, refinement, and growth of grains [61].

Figure 2.8 shows the evolution of the microstructure of AZ31B magnesium alloy during tensile loading to different strain levels at  $300^\circ\text{C}$  and a strain rate of  $10^{-3} \text{ s}^{-1}$ . The microstructure was observed for heated specimens at true strains of 0, 0.2, 0.4, and at failure (0.6 mm/mm). The influence of the temperature homogenization time (30 min at  $300^\circ\text{C}$ , without applied loading) was examined. Figure 2.8a) shows that at  $300^\circ\text{C}$ , specimens heated for 30 min without applying a load did not experience significant changes to their microstructures. Figure 2.8b) shows that at a strain of 0.2, coarser grain boundaries are present and small grains start to nucleate near the grain boundaries where the dislocation density is the highest. At a strain of 0.4, an increase in the number of small grains is observed as can be seen in figure 2.8c). Such smaller grains seem to indicate the prevalence of DRX as a major deformation mechanism. Finally, at failure (figure 2.8d), a complete reorganization of the microstructure is observed: smaller and equiaxed grains with fine borders constitute the totality of the material. A better

illustration of the change in average grain size at fracture as function of the strain at 300°C can be seen in figure 2.9. The evolution of the grain size shows a grain growth at 0.2 strain followed by a fast decrease of the grain size until the strain of 0.4. Finally, between 0.4 and 0.6 strains, the rate of grain-size refinement decreases.



**Figure 2.8** Evolution of the microstructure during tensile deformation at  $10^{-3} \text{ s}^{-1}$  and  $300^\circ\text{C}$  at different deformation levels: a) 0, b) 0 + 30 min heating at  $300^\circ\text{C}$ , c) 0.2, d), 0.4, and e) 0.6.



**Figure 2.9** Average grain size as function of the strain for tensile deformation at  $10^{-3} \text{ s}^{-1}$  and  $300^\circ\text{C}$ .

The effect of the temperature on the microstructure is shown in figure 2.10. The figure shows the microstructures obtained deforming at  $10^{-3} \text{ s}^{-1}$  until a strain level of 0.2 and for RT and  $300^\circ\text{C}$ . The observations at the RT are consistent with twinning indicating that twinning is a major deformation mechanism at low temperatures. These features might be expected given the imposed test conditions as discussed in section 2.3.1. At  $300^\circ\text{C}$ , smaller and more equiaxed grains are observed, which could correspond to DRX. The observations are consistent with the nucleation of new smaller grains, which could be expected for such loading conditions.

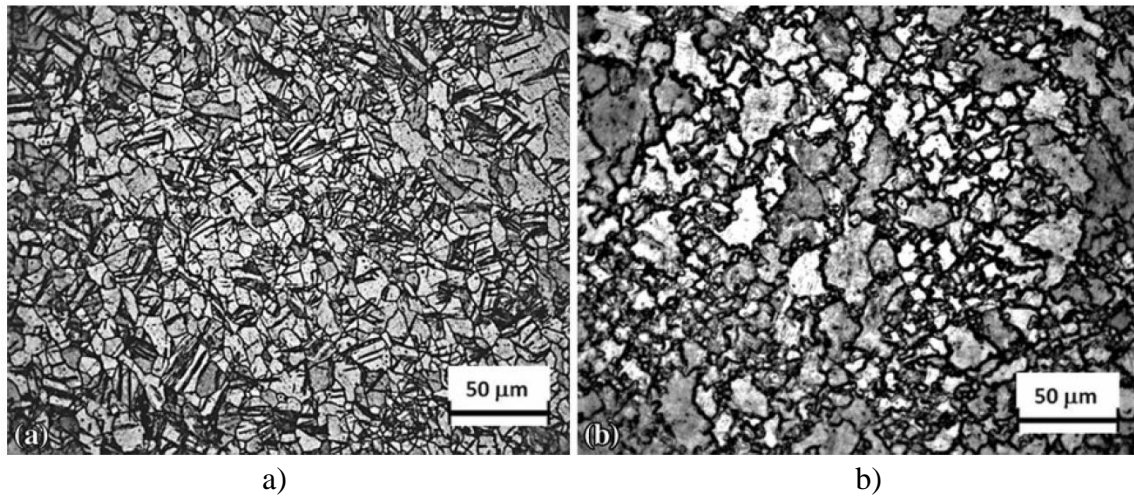


**Figure 2.10** Evolution of the microstructure during tensile deformation at  $10^{-3} \text{ s}^{-1}$  at: a) RT and; b) at  $300^\circ\text{C}$ .

#### *Static evolution of the microstructure*

Various as-rolled samples were heat treated at temperatures between  $100$  and  $475^\circ\text{C}$  for the analysis of static grain growth. The effects of both the annealing temperature and the annealing time were studied. The effect of the annealing temperature after  $8 \text{ h}$  of treatment is shown in figure 2.11: While there is not a significant difference in the size and configuration of the grains after treating at  $100^\circ\text{C}$  compared with the as-received microstructure (figure 2.6a), there is a significant change in the microstructure of AZ31B after heat treatment above  $300^\circ\text{C}$ . The original grain size was increased by  $385\%$  after  $8 \text{ h}$  of heat treatment at  $475^\circ\text{C}$ , growing from  $8.2 \pm 0.3$  to  $32 \pm 2 \mu\text{m}$ . Figure 2.12 shows the evolution of the grain size with temperature after  $8 \text{ h}$  of treatment. The figure shows that up to a temperature around  $300^\circ\text{C}$ , the grain size increases at a relatively low rate; however, significantly higher grain growth rate is

observed for temperatures greater than 300°C. This implies that 300°C is approximately the critical temperature that triggers the static recrystallization mechanism. The effect of the annealing time can be observed in Figure 2.13. No significant changes in the grain size or configuration were noted after 30 min and 1 h of annealing at 475°C. However, after 5 h, substantial grain growth is visible, reaching an average grain size of  $22\pm 2\ \mu\text{m}$ , with a broad grain-size distribution. Moreover, after 8 h, a higher percentage of grains is observed, considerably larger than those observed at 5 h, with an average grain size of  $32\pm 2\ \mu\text{m}$ .

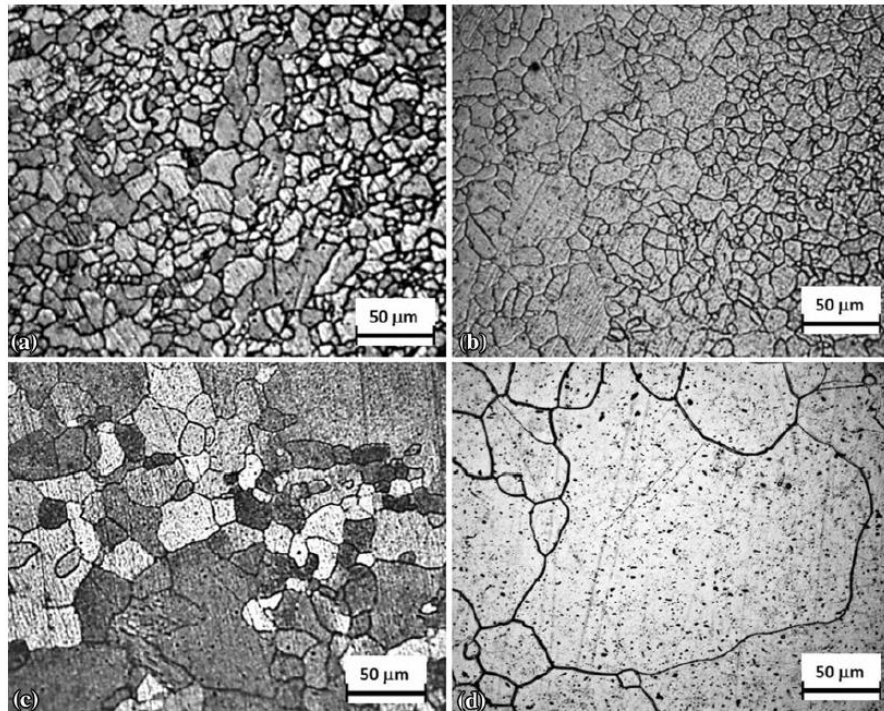


**Figure 2.11** Evolution of the microstructure after 8 h of annealing at different treatment temperatures a) as-received, b) 100°C, c) 300°C, d) 375°C, and e) 475°C

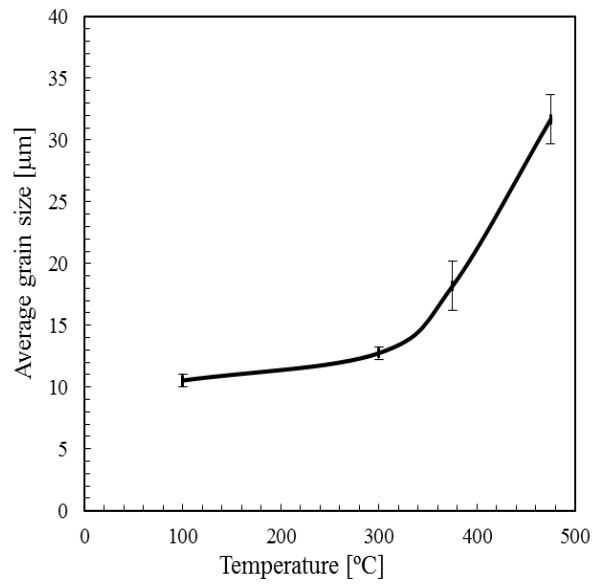


**Figure 2.12** Average grain size in function of temperature after 8 h of annealing

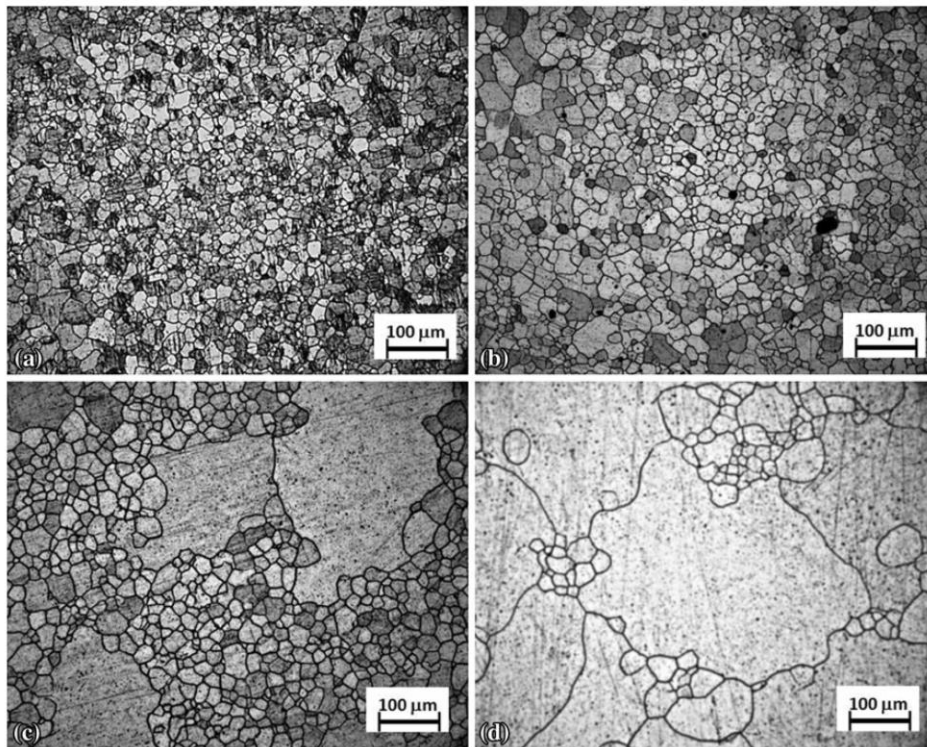


**Figure 2.13** Evolution of the microstructure after annealing at 475°C for the following times: a) 30 min, b) 1 h, c) 5 h, and d) 8 h.

## 2.4 Conclusions

Characterization of AZ31B twin-rolled cast wrought sheets was performed through tensile testing and microscopy analysis. From the results obtained, it can be concluded as follows:

1. At RT, an increase on the strain rate from  $10^{-4}$  to  $10^{-1} \text{ s}^{-1}$  does not affect the maximum strength. The elongation to fracture is just slightly increased with decreasing strain rates.
2. At  $300^\circ\text{C}$ , the strain rate has a major influence on the mechanical behavior of AZ31B. Decreasing the strain rate from  $10^{-1}$  to  $10^{-4} \text{ s}^{-1}$  results in a decrease of the maximum strength of 79% and increases the elongation to fracture in 78%.
3. Twinning is one of the main active deformation mechanisms at RT. Observations consistent with twinning also present at  $100^\circ\text{C}$ , but at a lower density.
4. DRX is present at temperatures beyond  $200^\circ\text{C}$ . At  $300^\circ\text{C}$  and  $10^{-3} \text{ s}^{-1}$ , the microstructure is completely recrystallized. At  $300^\circ\text{C}$  and  $10^{-4} \text{ s}^{-1}$ , the refinement of grains stops and grain growth occurs. The combination of high temperature and low strain rate favors GBS that leads to grain growth.
5. The rate-controlling mechanism during deformation of AZ31B are grain boundary diffusion in the range of  $100\text{-}200^\circ\text{C}$  and lattice diffusion at  $200\text{-}300^\circ\text{C}$

6. Heat-treatment experiments showed that the material experiences static grain growth when exposed to elevated temperatures for an extended period of time, with the highest growth being observed for heat treating for 8 h and 475°C.

## CHAPTER III

### DAMAGE AND FRACTURE OF TRC AZ31B MAGNESIUM ALLOY AT VARIOUS STRAIN RATES AND TEMPERATURES

#### 3.1 Introduction

Magnesium and its alloys are structural metals of special interest for the aerospace and automotive industries due to their high specific strength, leading to lighter structures and energy savings. However, wide spread use of magnesium alloys is hindered by their poor ductility and formability caused mainly by high  $c/a$  ratio of their HCP structure. Studies on magnesium alloys have focused on their mechanical properties, deformation mechanisms, texture evolution, processing and alloying systems. In general, the fracture behavior of magnesium and its alloys will depend on a number of factors, including: loading conditions such as temperature, strain rate, and triaxiality as well as internal factors such as grain size, and orientation. The ductility of the material is improved by increasing the temperature, and decreasing strain rate, as the number of active deformation mechanisms increases [10, 25, 62, 63]. However, despite the efforts in such areas, there are limited studies on work of fracture ( $W_f$ ) and damage of magnesium alloys. The work to fracture ( $W_f$ ) indicates the ability of the material to absorb energy up to fracture and it is an indicator of crashworthiness. Xu et al. [64], studied the effect of strain rate on energy absorption of extruded AM30, finding that the work to obtain a nominal deformation of 0.1 increases with an increasing strain rate and decreasing temperature, while decreases. They concluded that is mainly dominated by

the sensitivity of the yield stress, while is controlled by the total elongation to fracture. Ahmad et al. [65] concluded that the energy absorption of AZ91D is dependent on both strain rate and temperature: it increases with increasing strain rate and slightly decreases with increasing temperature.

Studies investigating the damage mechanisms of magnesium alloys are also scarce. It has been reported in the literature that second phase particles, grain boundaries and twined grains act as preferred damage initiation sites[13, 66-68]. Propagation of cracks has been studied just by few recent research works [66, 69-72]. Findings of such works conclude that crack propagation on magnesium alloys depends strongly on factors like original microstructure, and are mainly focused on fatigue crack propagation. However, the effect of strain rate and temperature on damage has been left unexplored. Most of the studies on damage mechanisms in magnesium alloys focused on a unique strain rate, mostly between  $10^{-4}$  and  $10^{-3} \text{ s}^{-1}$  [73, 74], and or superplastic conditions (high temperatures, low strain rates).

In order to guide future studies in selecting the alloying systems and designing forming processes a better understanding of the energy absorption and damage process is of high interest. With this goal in mind, this study explores the damage behavior of twin roll cast (TRC) AZ31B magnesium alloy plates subjected to tensile loading at different strain rates and temperatures. This paper is organized as follows; in section 4.2 the experimental methods used to conduct this study are presented. The results of the experimental investigations are presented in section 4.3. The results are then discussed in section 4.5. Finally, summary of the findings and concluding remarks are given.

### 3.2 Experimental Method

#### *Material*

The material used in this study is a twin roll cast (TRC) AZ31B plate rolled to a 3mm thickness and supplied by POSCO. The chemistry of the magnesium alloy was obtained through energy dispersive x-ray analysis (EDS). The composition in wt.% is as follows: Mg 95.4%, Al 3.32%, Zn 0.803%, Mn 0.304%, and Si 0.147%. The plate has three principal directions: rolling or longitudinal (L), transverse (T) and through thickness or short transverse (S) (figure 3.1).

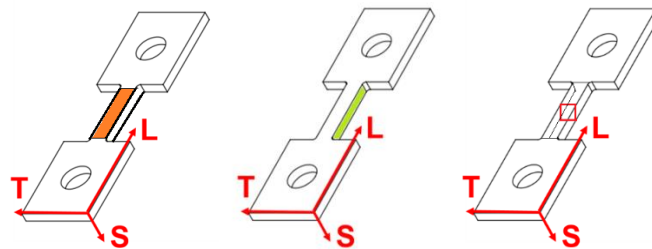


**Figure 3.1** Tensile specimen geometry and reference coordinates: longitudinal (L), transversal (T), through thickness or short transversal (S). The three studied planes: TS, LT and LS.

The initial microstructure of the material was obtained through grinding with SiC paper and polished with diamond and colloidal silica suspensions. For etching, an acetic-picric solution, with a 5:2 acetic-to-picric acid ratio was used. The initial microstructure of the LT and LS views are presented in figure 2. The material had an initial average

grain size 8.2  $\mu\text{m}$  in the LT plane and 11.2  $\mu\text{m}$  in the LS plane. The initial orientation of the material was obtained through Electron Backscatter Diffraction Analysis EBDS. The as-received plate exhibits a basal texture with the basal planes parallel to the LT plane as shown in the pole figures; figure 3.2.

### *Tensile tests*

Tensile specimens were machined according to the geometry in figure 3.1, with the loading axis parallel to the rolling direction. Tensile test were conducted at strain rates between  $10^{-4}$  and  $10^{-1} \text{ s}^{-1}$  and temperatures between room temperature (RT) and  $300^\circ\text{C}$ . The tests were conducted using a MTS Insight 30 kN equipped with a ThermoCraft environmental chamber. In order to achieve a constant strain rate, the crosshead speed was set to change according to the change in crosshead displacement. The samples were kept in the environmental chamber for 30 minutes before the test, in order to achieve homogenous heating of the specimen. Ultimate tensile strength (UTS) and elongation to fracture  $\epsilon_L$  were obtained from the stress-strain curves.  $\epsilon_L$  was calculated according to equation (3.1):

$$\epsilon_L = \log \left( \frac{L_f}{L_0} \right) \quad (3.1)$$

where  $L_0$  and  $L_f$  are the initial and final gage length of the tensile specimens.

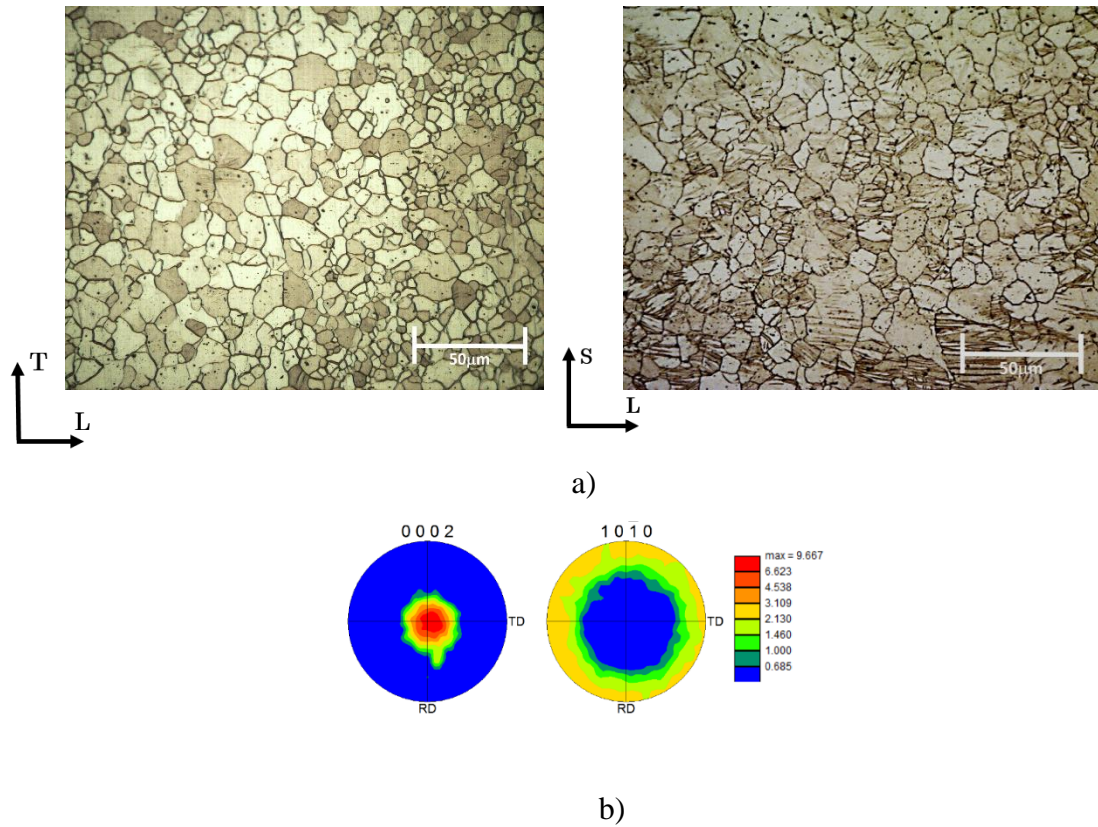


**Figure 3.2** a) Initial microstructure in the LT and LS planes and b) Initial orientation of the material.

The strain to failure  $\bar{\epsilon}_f$  was calculated as follows:

$$\bar{\epsilon}_f = \log \left( \frac{w_f t_f}{w_0 t_0} \right) \quad (3.2)$$

where  $w_o$  and  $w_f$  are the average of the initial and final width of the specimen, respectively; and  $t_o$  and  $t_f$  are the average initial and final thickness, respectively. The lateral strains were defined as:

$$\varepsilon_T = \log \left( \frac{t_f}{t_0} \right) \quad (3.3)$$

$$\varepsilon_s = \log \left( \frac{W_f}{W_0} \right) \quad (3.4)$$

The work to fracture  $W_f$  was obtained by integrating the area under the nominal stress-strain curves:

$$w_f = \int_0^{\varepsilon_L} \sigma \, d\varepsilon \quad (3.5)$$

where  $\varepsilon_L$  the elongation to fracture and  $\sigma$  is the nominal stress.

For interrupted tests; the tensile tests were stopped at the nominal strain to failure initiation, which we define as the nominal strain at the onset of abrupt decrease in nominal stress. Laser extensometer was used to measure the strain to failure initiation at which the tests were stopped.

### *Fractography*

In order to carry out a thorough analysis on the damage and fracture mechanisms of AZ31B under tensile loading, three different types of microstructural observation were explored:

- i) SEM observation of fracture surfaces; TS planes were analyzed (figure 3.1).
- ii) Optical microscope observation of the post-mortem specimens in the LS and LT planes. Initially, the surface of the corresponding plane was grinded and

polished. The prepared surfaces were then observed through an optical microscope and micrographs were taken, with special interest in damage features. Later, the samples were etched with an acetic/picral solution, and the surface of interest observed again through an optical microscope. Afterwards, the mid-section of the specimen was analyzed. To this purpose, the sample was grinded with 1200 SiC paper while cooled with water, until reaching the thickness corresponding to the mid-section of the specimen. This sample was polished, micrographs were taken, and it was consequently etched and observed again.

- iii) Optical microscope observation of interrupted test specimens (at selected conditions that will be discussed further on in this paper) in the LS, LT and TS planes. For this purpose, three tensile tests (for analysis of each plane of interest) were interrupted at the strain of imminent failure (which was deduced from tests performed to complete fracture). Both surfaces and mid-sections of the LS and LT planes, as well as the mid-section of the TS plane were prepared according to the method described previously in this section.

### **3.3 Results and Discussion**

#### *Flow behavior*

The mechanical response of TRC AZ31B under tension at different temperatures and strain rates is shown in figure 3.3. It is worth noting that the stress-strain values

presented are nominal, since measurement of strain beyond necking was impeded due to the inhomogeneity of the deformation.

As general trend, increasing strain rate causes an increase in the flow stress and a decrease in the elongation to failure. However, the extent at which the strain rate affects the mechanical response depends on the strain rate sensitivity and its evolution with temperature. At room temperature, the effect of the strain rate on the flow stress is negligible and a small change of the UTS is observed (figure 3.3a). However, the elongation to failure shows certain sensibility to strain rate variation. At 100°C (figure 3.3b) the strain rate sensibility appears to be higher. Consequently, a bigger decrease in the flow stress and higher elongation to fracture are found with decreasing strain rates. At 300°C (figure 3.3c) the strain rate sensitivity is highest, with 84% decrease in the flow stress and a 100% increase in the strain to failure when the strain rate is decreased from  $10^{-1}$  to  $10^{-4}$  s<sup>-1</sup>.

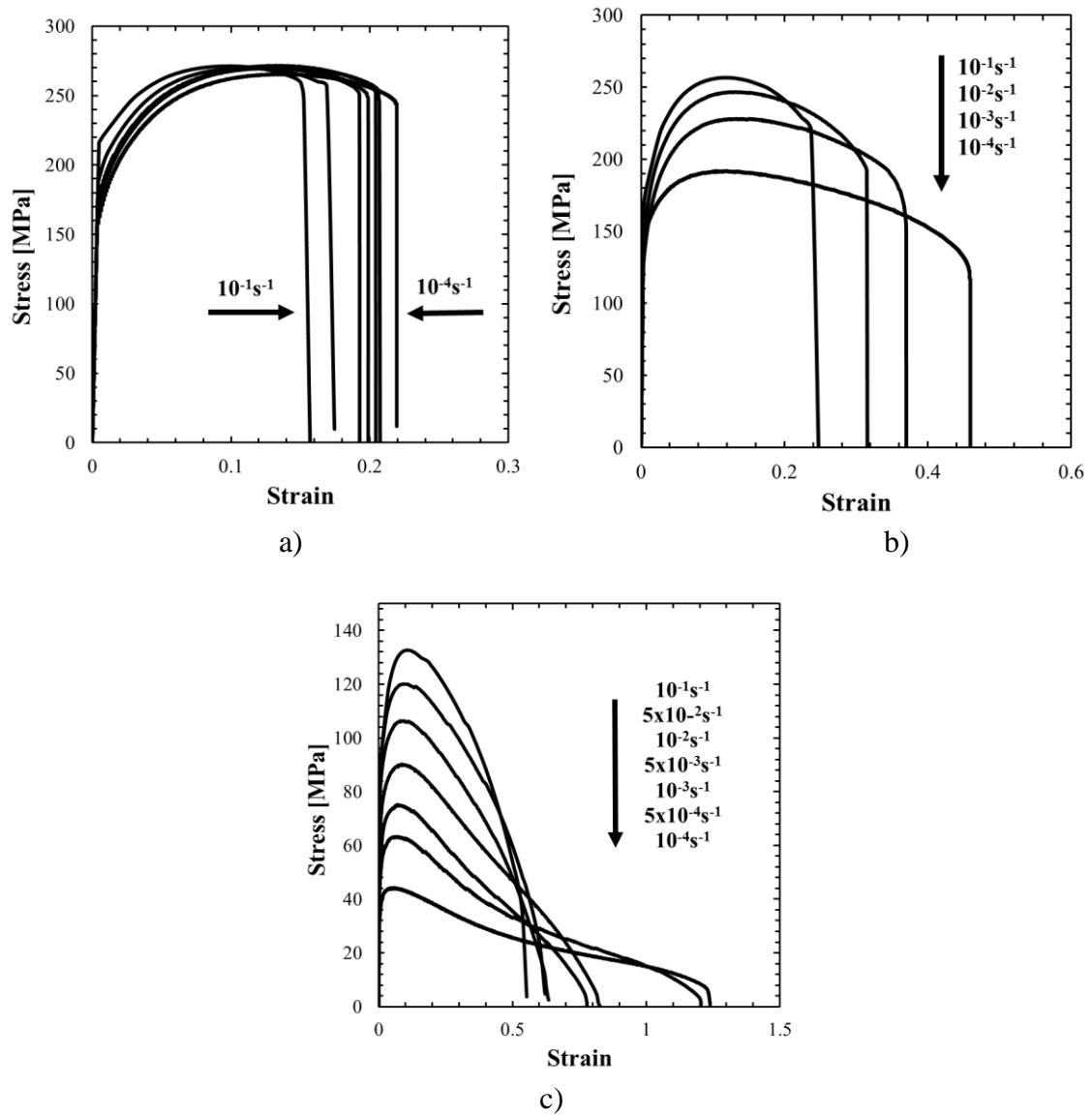
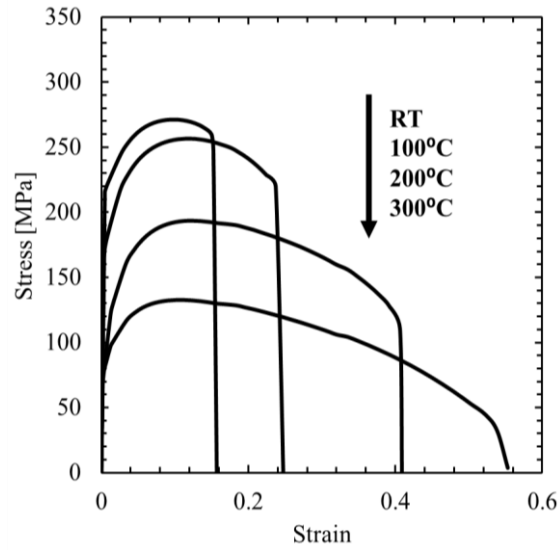


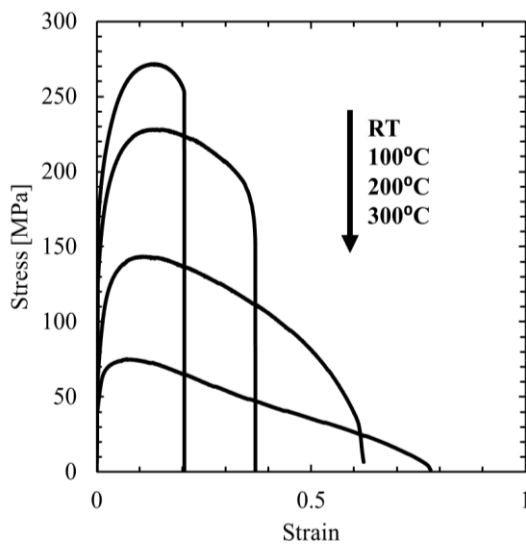
**Figure 3.3** Engineering stress vs strain curves of TRC AZ31B plates under tensile tests at various strain rates and: a) room temperature (RT), b) 100 and c) 300°C.

The effect of temperature on the stress-strain curves of AZ31B is presented in figure 3.4. As a general trend, for a constant strain rate, the increase of temperature induces a thermal softening of the material, along with an increase of the elongation to failure. The effect of thermal softening is more pronounced as strain rate decreases.

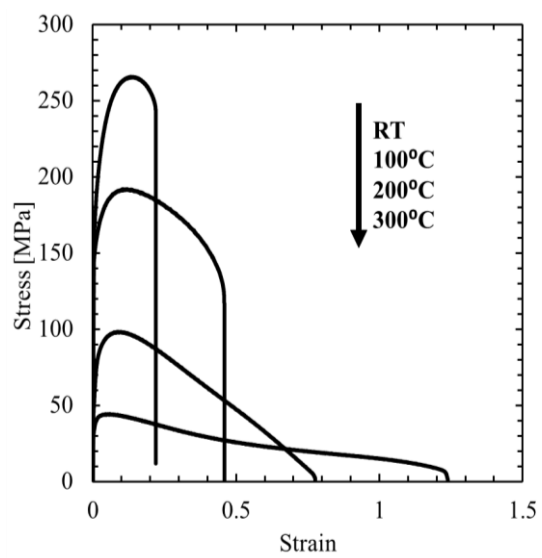
The strain to failure  $\epsilon_f$  (i.e., the strain in the cross sectional area after complete failure) is plotted in function of strain rate and temperature in figure 3.5. Figure 3.5a shows that a small  $\epsilon_f$  is achieved at low temperatures.  $\epsilon_f$  has a low strain rate sensitivity at RT and 100°C. Higher temperatures and low strain rates result in higher  $\epsilon_f$ . At 200 and 300°C higher  $\epsilon_f$  is achieved as well as a higher strain rate sensitivity. Figure 3.5b shows a high temperature sensitivity of  $\epsilon_f$ . Temperature sensitivity of  $\epsilon_f$  seems to be equal across all the strain rate studied, in contrast with the strain rate sensitivity of  $\epsilon_f$ , which depends deeply on the temperature considered.



a)



b)



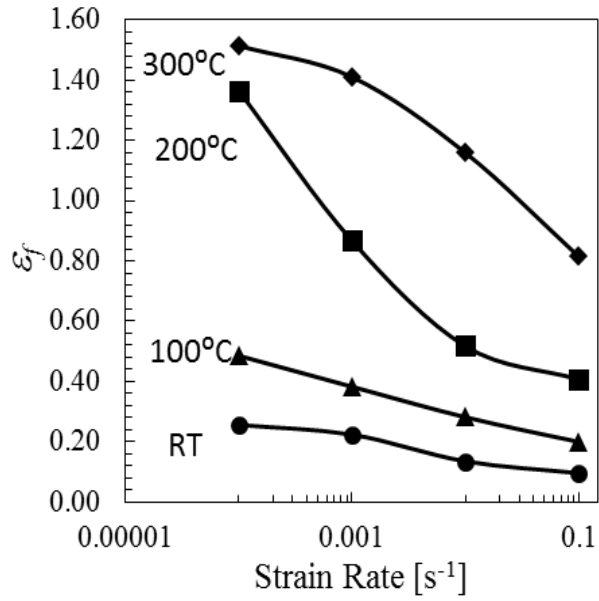
c)

**Figure 3.4** Engineering stress vs strain curves of TRC Z31B plates under tensile tests at a)  $10^{-1}$ , b)  $10^{-3}$  and c)  $10^{-4} \text{ s}^{-1}$  at various temperatures.

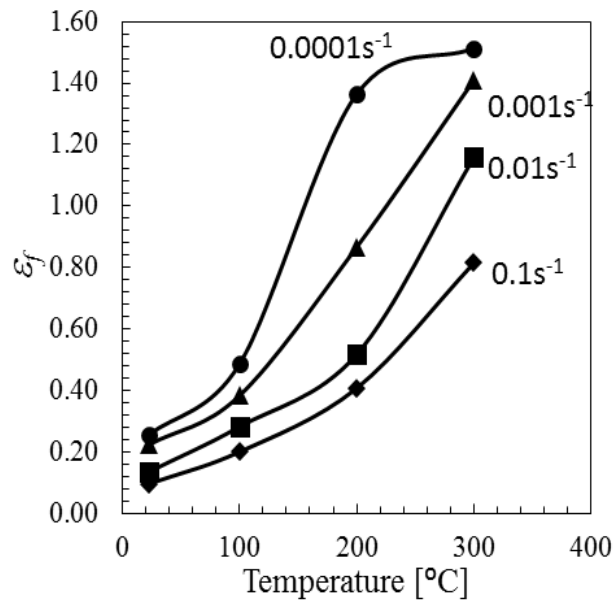
Due to the anisotropic behavior of magnesium plates,  $\epsilon_f$  was broken down into components in the S direction ( $\epsilon_S$ ) and the T direction ( $\epsilon_T$ ) and its evolution with strain rate is plotted in figure 3.6. The comparison of figures 3.6a and 3.6b clearly highlight the different contribution of the strains in the S and T direction to the total  $\epsilon_f$ .  $\epsilon_S$  changes significantly with temperature (figure 3.6a). At low temperatures (RT and 100<sup>0</sup>C) the strain along the S direction is minor and increases slightly with strain rate. However, at 200 and 300<sup>0</sup>C the rate at which  $\epsilon_S$  increases with strain rate is much higher than that at lower temperature. Strain increases up to 700% with reduction of strain rate from 10<sup>-1</sup> to 10<sup>-4</sup> s<sup>-1</sup> at 200 and 300<sup>0</sup>C.

#### *Fracture behavior*

With the aim of studying the initiation of damage in magnesium under tensile loading, a selection criteria of the most relevant loading conditions was needed. As temperature and strain rate exhibited a significant effect on both strain to failure and flow stress. Therefore, it was necessary to choose a significant parameter accounting for

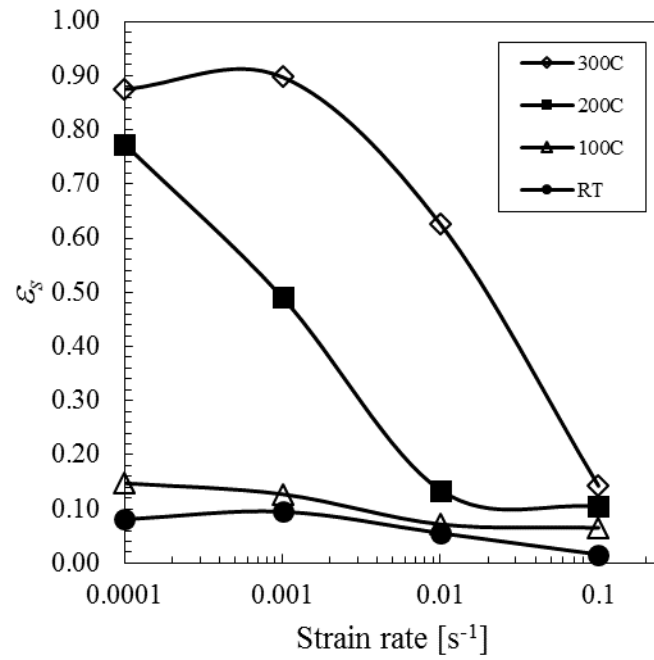


a)

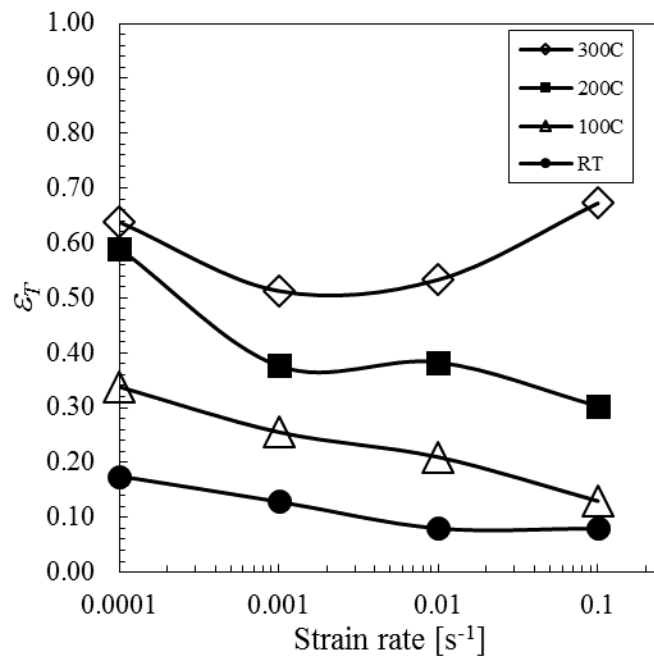


b)

**Figure 3.5** Strain to failure  $\epsilon_f$ : a) vs strain rate, b) vs temperature.



a)



b)

**Figure 3.6** a) Strain along the S direction  $\varepsilon_S$  vs strain rate and b) Strain along the T direction  $\varepsilon_T$  vs strain rate.

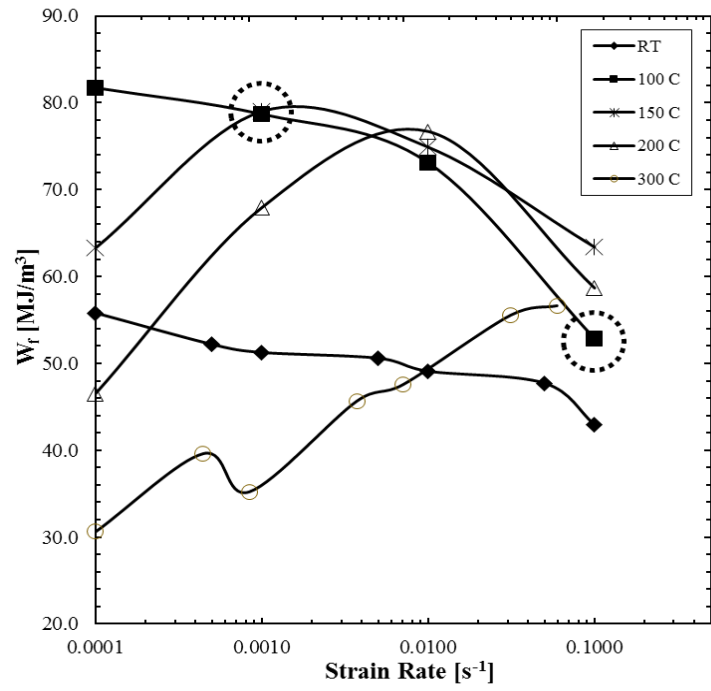
both strain rate and temperature effects. Thereby, the work of fracture ( $W_f$ ) was proposed as selection criteria since it takes into account the effect of loading conditions on both flow stress and elongation to fracture.

Based on the stress-strain curves (figures 2.2, 3.3, 3.4) the work of fracture ( $W_f$ ) was calculated according to equation (3.5). It is observed in figure. 3.7a that the evolution of the work to fracture in function of the strain rate  $W_f$  depends on temperature. At low temperatures, (RT and 100°C), the work to fracture decreases with increasing strain rate. However, at 100°C, an abrupt drop of the  $W_f$  occurs at high strain rates. For the moderate temperatures range (150-200°C) the work to fracture increases with increasing strain rate, and reaches a maximum between  $10^{-2}$  and  $10^{-3} \text{ s}^{-1}$  then decreases at the high strain rate end. Finally, at 300°C, the  $W_f$  increases with increasing strain rate. Figure 3.7b illustrates, for a given strain rate, the work to fracture as a function of temperature  $W_f(T)$ . All the curves present a similar trend, with a maximum  $W_f$  at temperatures between 100-200°C. It is noted from figure 3.7b that the  $W_f$  values for  $10^{-1} \text{ s}^{-1}$  are lower than those of lower strain rates.

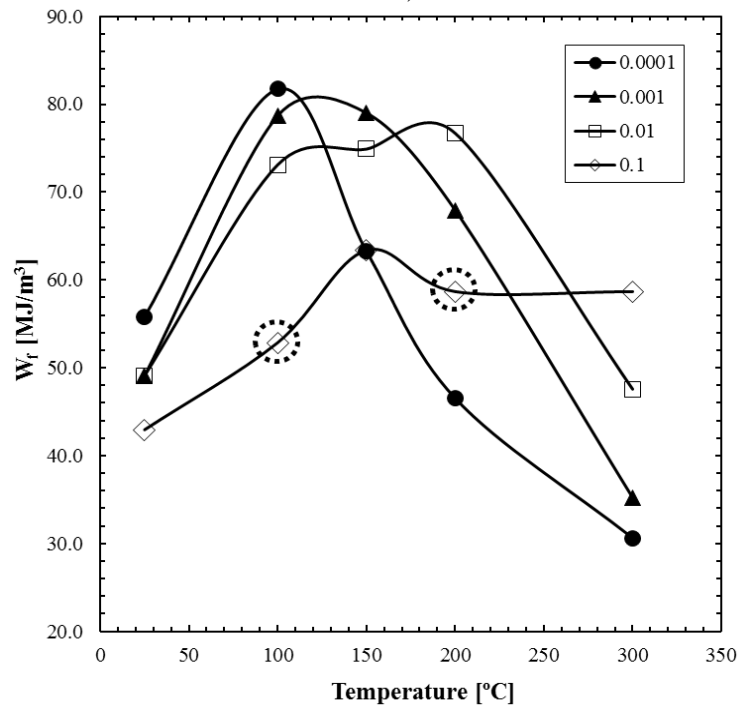
Strain rate and temperature will affect the work of fracture in different manners:  $W_f$  values are calculated from flow stress and elongation to fracture. The temperatures and strain rates that lead to low flow stress and therefore decrease of  $W_f$ , are the same that lead to higher elongation to fracture, increasing  $W_f$ . Therefore, the evolution of the work to fracture is affected by: i) strain rate sensitivity of elongation to fracture and flow stress, ii) the ability of the material to undergo thermal softening and iii) the interconnection between the different phenomena.

Consequently, the three distinguishable  $W_f$  trends in figure 3.7a can be described as follows: i) at low temperatures the strain rate sensitivity of the elongation to failure dominates, resulting in a  $W_f$  decrease with increasing strain rate; ii) in the moderate temperature range,  $W_f$  reaches a maximum at certain strain rates, indicating the presence of the competing phenomena described above; iii) at high temperature, the strain rate sensitivity of the flow stress dominates, and therefore  $W_f$  increases with increasing strain rate.

The evolution of  $W_f(T)$  equally evidence the existence of a competition between the two phenomena: increase in strain to failure and the decrease in flow stress with increasing temperature. At low temperature, the sensitivity of the strain to failure dominates, while at temperatures beyond the critical temperature, the decrease in flow stresses controls  $W_f(T)$ .



a)



b)

**Figure 3.7** Work to fracture ( $W_f$ ) vs: (a) strain rate for various test temperatures, (b) temperature for various strain rate. Dotted circles indicate conditions selected for further studies.

Xu et al. [64] reported a decreasing  $W_f$  with increasing strain rate for AM30 tested at 100°C, for a strain rate range of 0.00075 to 9 s<sup>-1</sup>. Xu et al. also studied the effect of temperature on  $W_f$  within the range of -143 to 100°C, and reported increasing  $W_f$  with increasing temperature. They attributed this trend of  $W_f$  to the thermal softening of the material. Xu results are in accordance with the experimental observation in Fig. 3.7 for the RT-100°C range. Ahmad et al. [65], however, reported increasing work to fracture with increasing strain rate both at RT and 250°C. Although the velocity range covered in their study is very large (10<sup>-4</sup> to 1500s<sup>-1</sup>), only the extreme values of the range were taken into consideration. We believe that, if intermediate strain rates and temperatures had been studied, a maximum  $W_f$  would have been observed near 250°C.

Macroscopic features of fracture surfaces examined through SEM are shown in figures 3.8 and 3.9. At 100°C (figure 3.8), most of the deformation occurs in the T direction and it can be clearly observed that increasing the strain rate resulted mainly in a reduction of the strain along T. All the specimens examined failed by shear. The specimens tested at lower temperatures exhibited a slanted fracture and those tested at higher temperatures showed a very ductile fracture. Figure 3.9 illustrates the effect of the strain rate on the macroscopic features of fracture at 300°C. As expected, the strain increases with decreasing strain rate. However, and unlike its counterpart at 100°C, the strain along the S direction is higher than the strain along the T direction. The fracture mode at 300°C was very ductile.

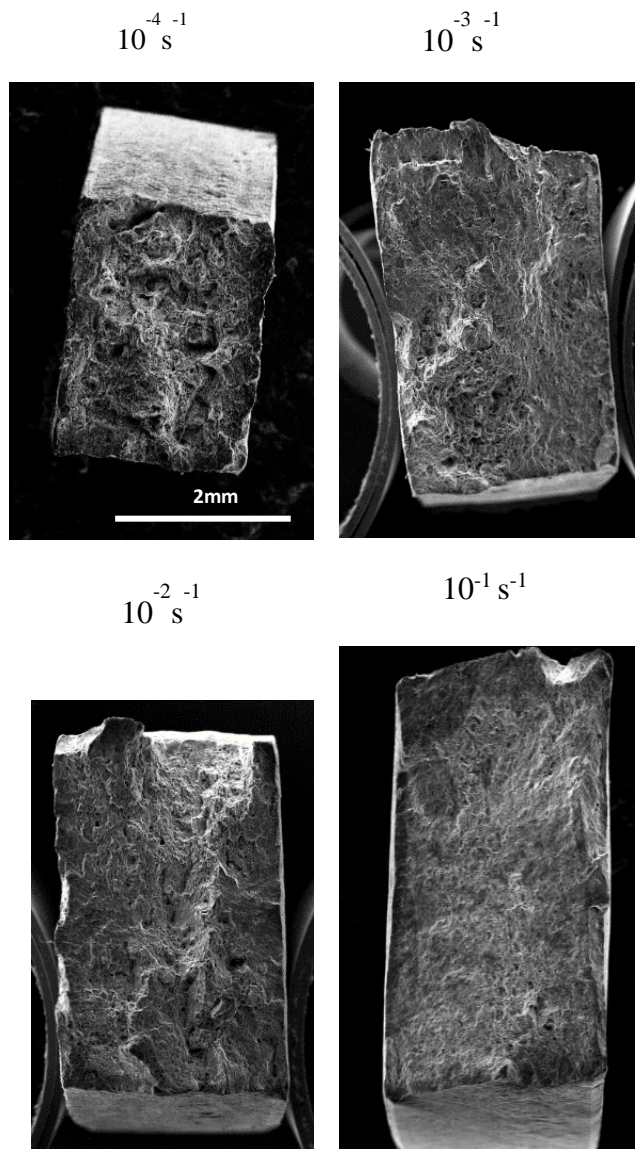


**Figure 3.8** Fracture surface of tensile specimen tested at various strain rates at 100°C.

The fracture surfaces obtained at 100°C and 300°C are significantly different. A higher reduction in area is evident at 300°C, as strain to fracture increases at higher temperatures. In contrast to the observations at 100°C, the strain is highest in the S direction at 300°C. As discussed previously, this effect is due to anisotropy of wrought magnesium and the activation of deformation mechanism at higher temperatures

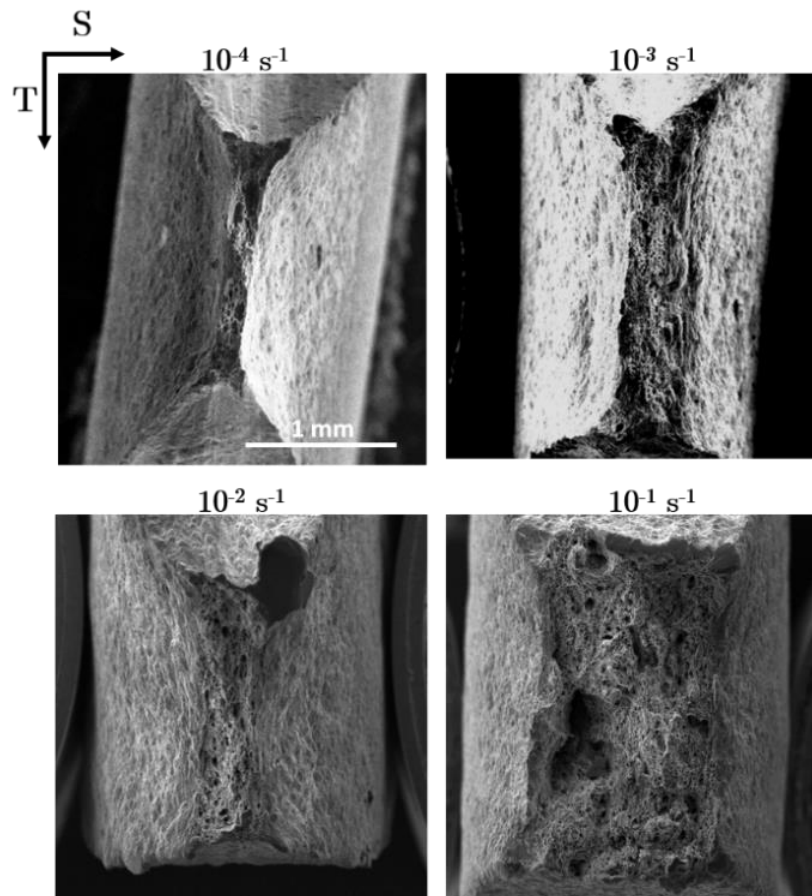


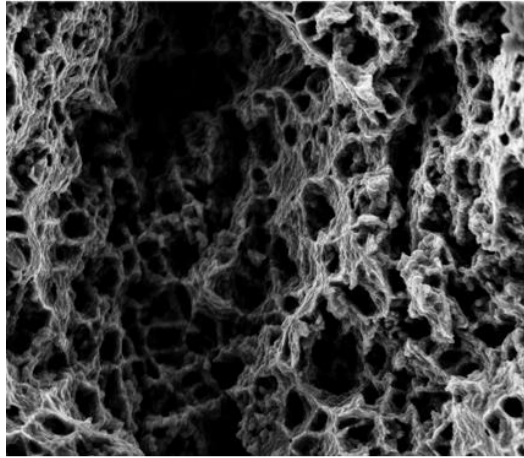
**Figure 3.9** Fracture surface of tensile specimen tested at various strain rates and 300°C.

Higher magnification micrographs in figures 3.10 and 3.11 show details of the fracture surface. The effect of strain rate at 200°C is illustrated in figure 3.10. At  $10^{-4} \text{ s}^{-1}$  (figure 3.10a) the surface shows deep dimples indicating a ductile fracture. As the strain rate increases (figure 3.10b) the size and depth of dimples decreases. Finally, at  $10^{-1} \text{ s}^{-1}$  (figure 3.10c) shallower and smaller dimples indicate a lower ductility, which correlates with our stress strain curves, hence a transition to a quasi-brittle fracture is evidenced.

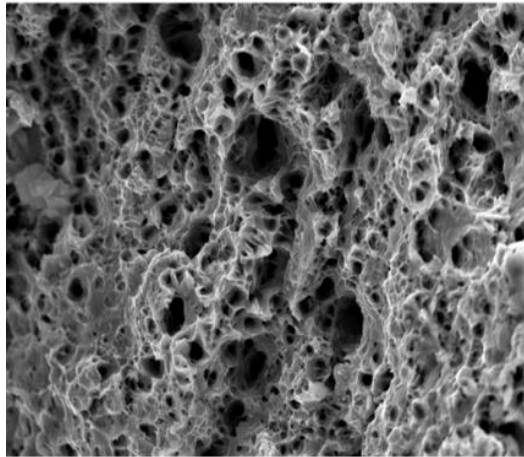
The effect of temperature on the microscopic morphology of fracture is shown in figure 3.11 for a strain rate of  $10^{-3} \text{ s}^{-1}$ . At RT and 100°C flat facets indicate a quasi-brittle behavior of the material. Increasing the temperature to 200 and 300°C induces a transition to ductile fracture, as the facets disappear and the surface is highly dimpled. As the test temperature increases, so does the density and depth of dimples.

In order to rationalize the difference between  $\epsilon_T$  and  $\epsilon_S$  with loading conditions we need to take into account the types of deformation mechanisms that are required to deform along each direction. Strain on the S direction cannot be easily accommodated at room temperature, since the mechanisms able to accommodate contraction of the c-axis (contraction twinning and pyramidal slip) have a relatively high critical resolved shear stress (CRSS). However, the activation of these mechanisms is favored at higher temperatures, resulting in increased strain along the S direction when the material is loaded at 300°C in comparison with lower temperatures. This effect of temperature on strain will also be obvious on fracture surface observations in section 3.2.

a)  $10^{-4} \text{ s}^{-1}$



b)  $10^{-3} \text{ s}^{-1}$



c)  $10^{-1} \text{ s}^{-1}$

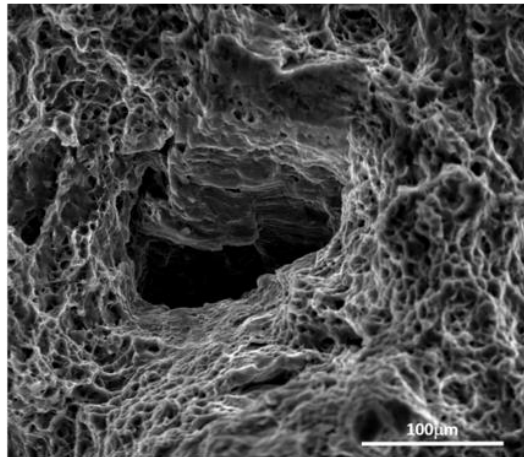


**Figure 3.10** Fracture surface of tensile specimen tested at  $200^{\circ}\text{C}$  and various strain rates.

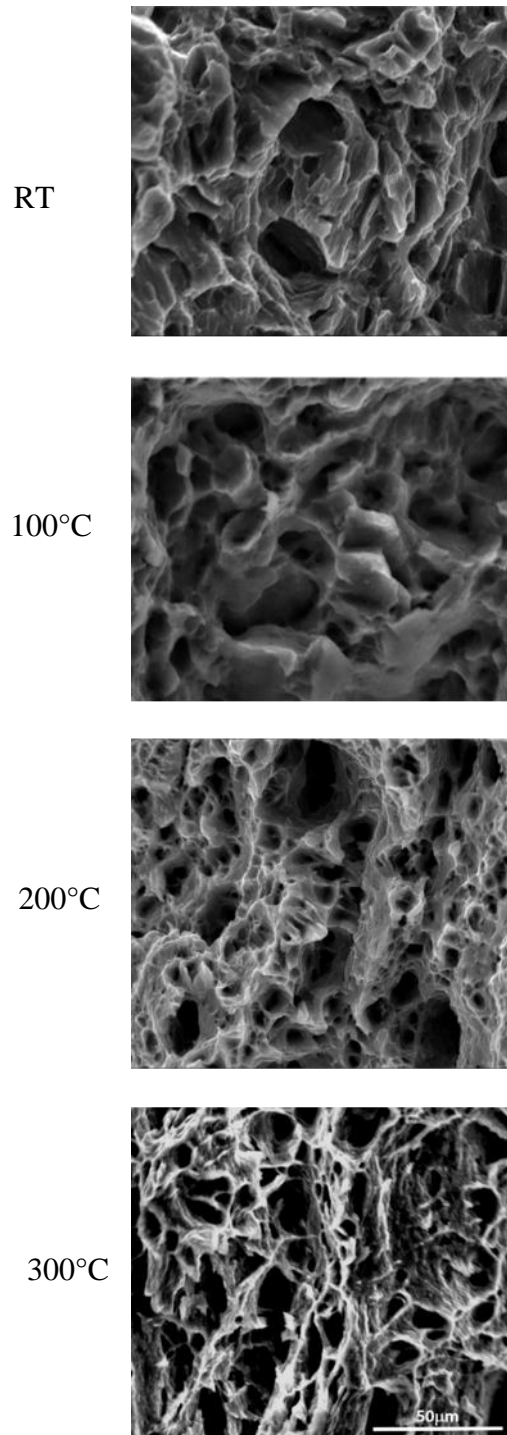


**Figure 3.11** Fracture surface of tensile specimen tested at  $10^{-3} \text{ s}^{-1}$  and various temperatures.

## *Damage*

In order to study the effect of strain rate and temperature in damage, the selected loading conditions to conduct microscopy analysis was based on the trends observed for the work of fracture ( $W_f$ ). Specifically, the loading conditions preceding and following the transitions of  $W_f$  were of interest (figures 3.7a and b). More precisely, to investigate the influence of strain rate on the damage processes, two strain rates at 100°C were selected:  $10^{-1}$  and  $10^{-3} \text{ s}^{-1}$ . The influence of temperature on the damage process was studied at a strain rate of  $10^{-1} \text{ s}^{-1}$  for 100 and 200°C.

The LS, LT and TS planes (figure 3.1) were studied. For brevity, only those corresponding to the LS and LT planes are shown, since these planes exhibited the most interesting features. Observations were made on the surface and the midsection of the specimens. In most of the cases, the surface and midsection exhibited similar features, and so only the surface landscape is shown. The instances where surface and midsection were different are indicated.

Figure 3.12 shows the LS and LT planes of specimens deformed at  $10^{-3}$  and  $10^{-1} \text{ s}^{-1}$  and at 100°C up to strain to failure initiation. The LS planes shown (figure 3.12a) correspond to the surface of the specimens. In figure 3.12b the LT plane of  $10^{-3} \text{ s}^{-1}$  corresponds to the midsection of the specimen (in this case, the surface of the  $10^{-3} \text{ s}^{-1}$  LT plane displayed a landscape similar to that shown of  $10^{-1} \text{ s}^{-1}$ ).

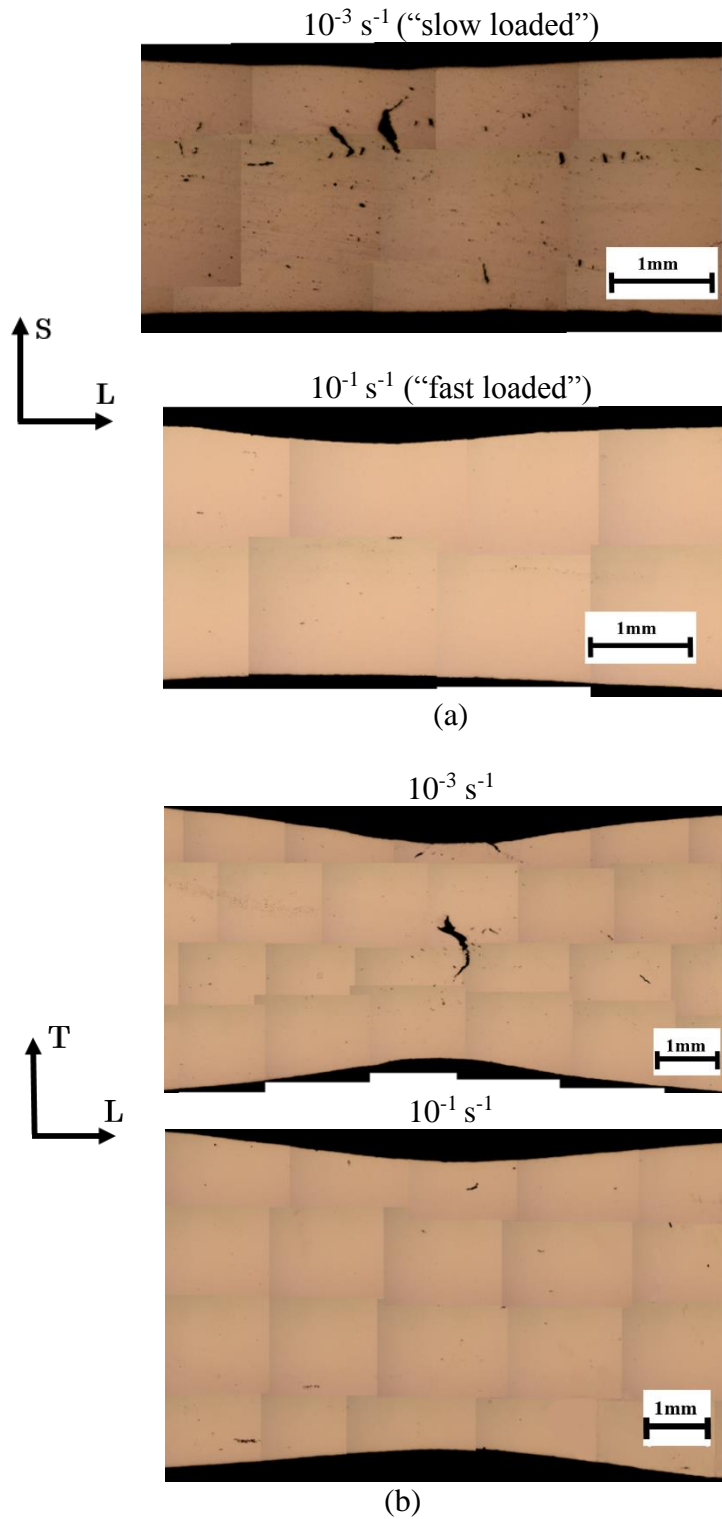


**Figure 3.12** OM micrograph of uniaxial tensile specimen interrupted at strain before failure at  $10^{-3} \text{ s}^{-1}$  and  $10^{-1} \text{ s}^{-1}$ : a) LS plane and b) LT plane

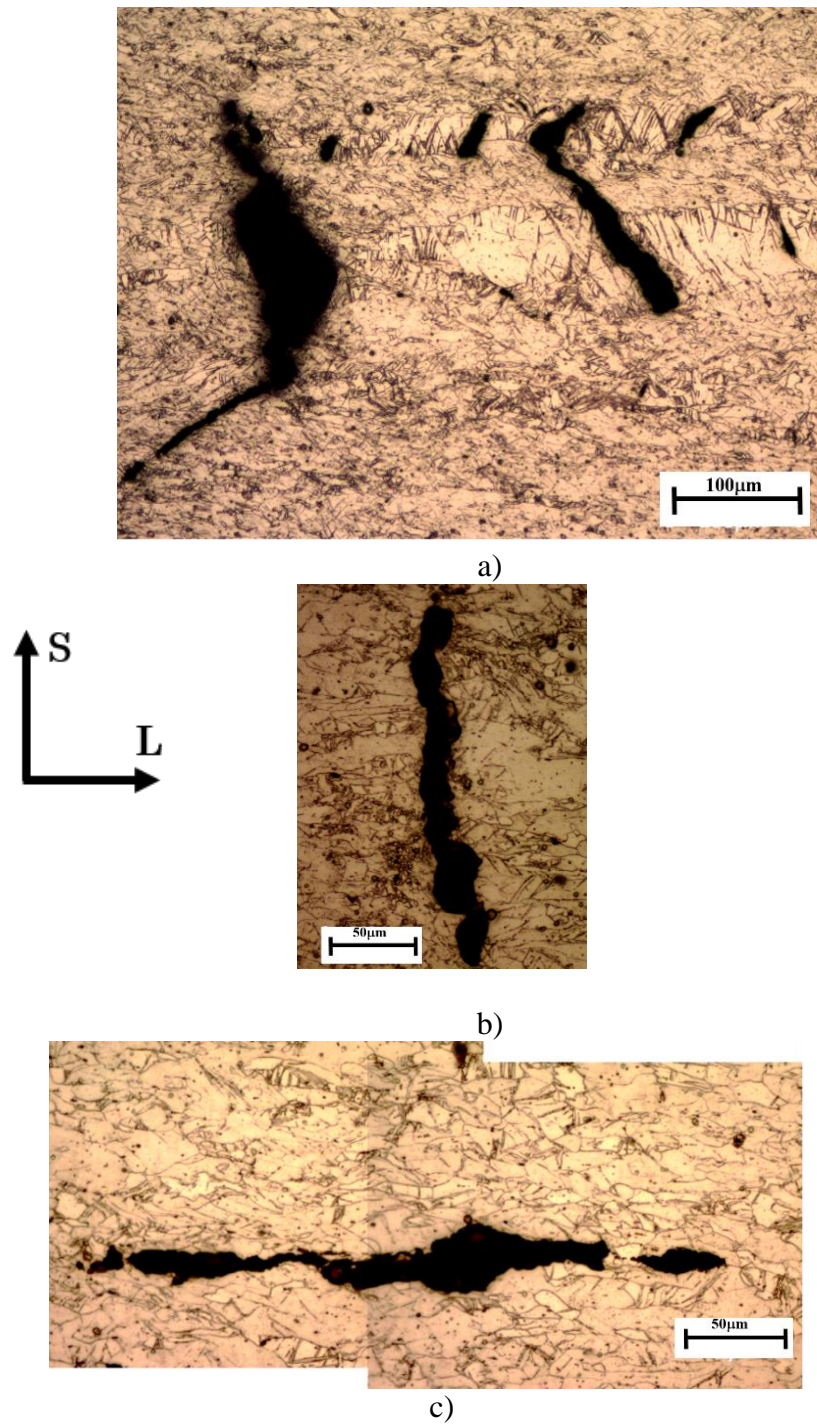
In figure 3.12a, the LS planes reveal a significant difference in the quantity and the size of micro-voids and cracks, as well as differences in the elongation direction of the cracks. The “slow loaded” specimen ( $10^{-3} \text{ s}^{-1}$ , figure 3.12a) shows cracks, of sizes up to 0.58mm, extending in two directions: parallel and perpendicular to the loading direction L. The LS plane of the “fast loaded” specimen ( $10^{-1} \text{ s}^{-1}$ , figure 3.12a), exhibits less micro-voids of smaller size than the slow loaded specimen, with few visible cracks elongated exclusively along the L direction.

Figure 3.12b displays the LT planes corresponding to  $10^{-1}$  and  $10^{-3} \text{ s}^{-1}$ . Firstly, by comparing with the LS planes in figure 3.12a, it is evident that, at  $100^\circ\text{C}$  the strain along the T direction is higher than the strain in the S direction. For the strain rate of  $10^{-3} \text{ s}^{-1}$ , the LS plane exhibits less number of micro-voids and micro-cracks compared to the LT plane in figure 3.12a. At the same time, the LS and LT plane corresponding to  $10^{-3} \text{ s}^{-1}$  have in common the presence of large cracks propagating in a zig-zag pattern. The LT plane of  $10^{-1} \text{ s}^{-1}$  is similar to its LS plane in the number and size of micro-voids, as well as in their elongation direction, mainly in the L direction.

Comparing the  $10^{-3}$  and  $10^{-1} \text{ s}^{-1}$  LT planes we can see that  $10^{-3} \text{ s}^{-1}$  displays more micro-voids and cracks than  $10^{-1} \text{ s}^{-1}$ , maintaining the trend observed for the LS planes.

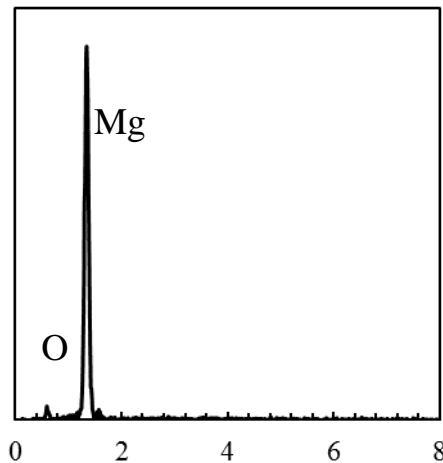
For a thorough investigation of the damage observed in Figure 3.12, the LS planes of the specimens were etched and the micrographs obtained are presented in Figure 3.13 and 3.14. For brevity, only the results for LS planes are shown (The etched micrographs obtained for the LT and TS planes can be found in the appendix).

Figure 3.13 shows the three types of micro cracks found in the LS plane of the specimen strained at  $10^{-3} \text{ s}^{-1}$ : i) cracks related to twins, elongated along the twinning bands as shown in figure 3.13a, where it is also observed the coalescence of micro-cracks formed in different twin bands; ii) micro-cracks propagating along the S direction but with no obvious correlation to twinning are presented in figure 3.13b; iii) micro-cracks propagating in the loading direction as observed in figure 3.13c, such micro-cracks have second phase particles as their nucleation sites [18]. This was corroborated through EDS analysis. The corresponding EDS spectra in Figure 3.14 indicates that at least some of the second phase particles involved in void nucleation are magnesium oxide (MgO)/intermetallics. The occurrence of such oxide-intermetallics in magnesium has been reported in the literature by Lugo et al. [21] and more recently by Kondori and Benzerga [18].

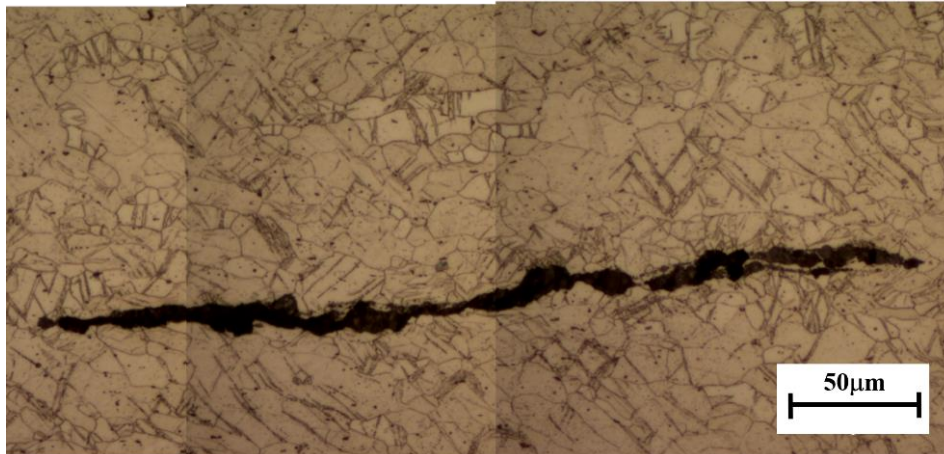


**Figure 3.13** OM micrograph of uniaxial tensile specimen tested interrupted at strain before failure at  $10^{-3} \text{ s}^{-1}$  showing: a) micro cracks propagated along twin bands, b) micro cracks parallel to the L direction, c) micro cracks perpendicular to the L direction.

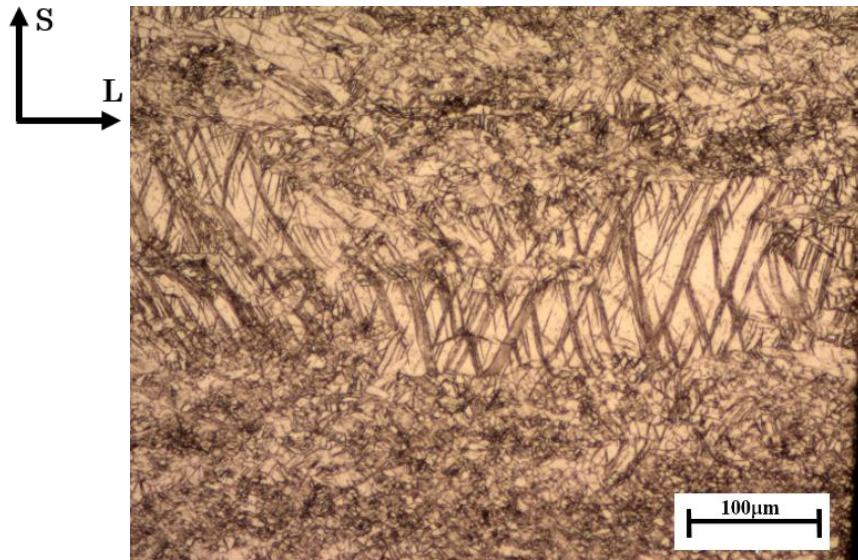
Details of the etched LS plane corresponding to  $10^{-1} \text{ s}^{-1}$  is presented in Figure 3.15. Figure 3.15a shows a crack representative of the ones found in this condition. It is elongated along the L direction, with no obvious correlation with the twin bands in the sample. Unlike the specimen loaded at  $10^{-3} \text{ s}^{-1}$ , no cracks associated with twinning were found. It is interesting to note that the absence of twin-nucleated cracks at  $10^{-1} \text{ s}^{-1}$  it is not a result of lack of twinning in the specimen, by the contrary, figure 3.15b shows the extent of twinning in the specimen. This is expected since, as mentioned in the previous chapter, twinning is promoted by high strain rates, as a mechanism that enables deformation in the absence of slip mechanisms. This fact will be topic of discussion later in this chapter. EDS analysis revealed traces of Al, Mg and Mn in some particles found in the cracks of the  $10^{-1} \text{ s}^{-1}$  (figure 3.16). According to the Mg/Al/Zn/Mn phase diagram [20], at 0.3% of Mn,  $\text{Al}_{11}\text{Mn}_4$  are possible precipitates for AZ31.



**Figure 3.14** EDS spectra for particles found in  $10^{-3} \text{ s}^{-1}$   $100^\circ\text{C}$  micro-voids.



(a)



(b)

**Figure 3.15** OM micrograph of the specimen tested at  $10^{-1} \text{ s}^{-1}$  and  $100^\circ\text{C}$ : a) Detail from an interrupted specimen; and b) Profuse twinning, however, no micro-voids are observed along twinning bands.

In order to further validate the damage observations, the microstructure of post-mortem samples was also analyzed in the LT plane. In this way, we will also be able to assure, for example, that the reason behind the limited damage observed at  $10^{-1} \text{ s}^{-1}$  is not related to an early interruption of the tensile test.

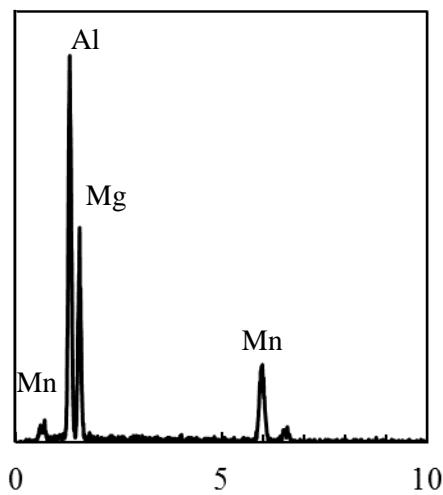


**Figure 3.16** EDS spectra for particles found in  $10^{-1}$   $100^\circ\text{C}$  micro-voids.

Figure 3.17 shows details of damage found in the post-mortem specimen corresponding to  $10^{-3} \text{ s}^{-1}$ . In the post-mortem specimen, coalescence of two of the three types of micro-cracks observed at imminent failure is evident (figure 3.17a): one nucleated at second phase particles, along L and one nucleated at twinning sites, along S, forming a bigger crack. Examination of the microstructure under the fracture surface (Figure 3.17b) revealed micro-cracks propagating parallel to the fracture surface. These

micro-cracks usually appeared along a direction forming an angle of approximately  $45^\circ$  with the loading direction, a characteristic that might indicate shear localization[75].

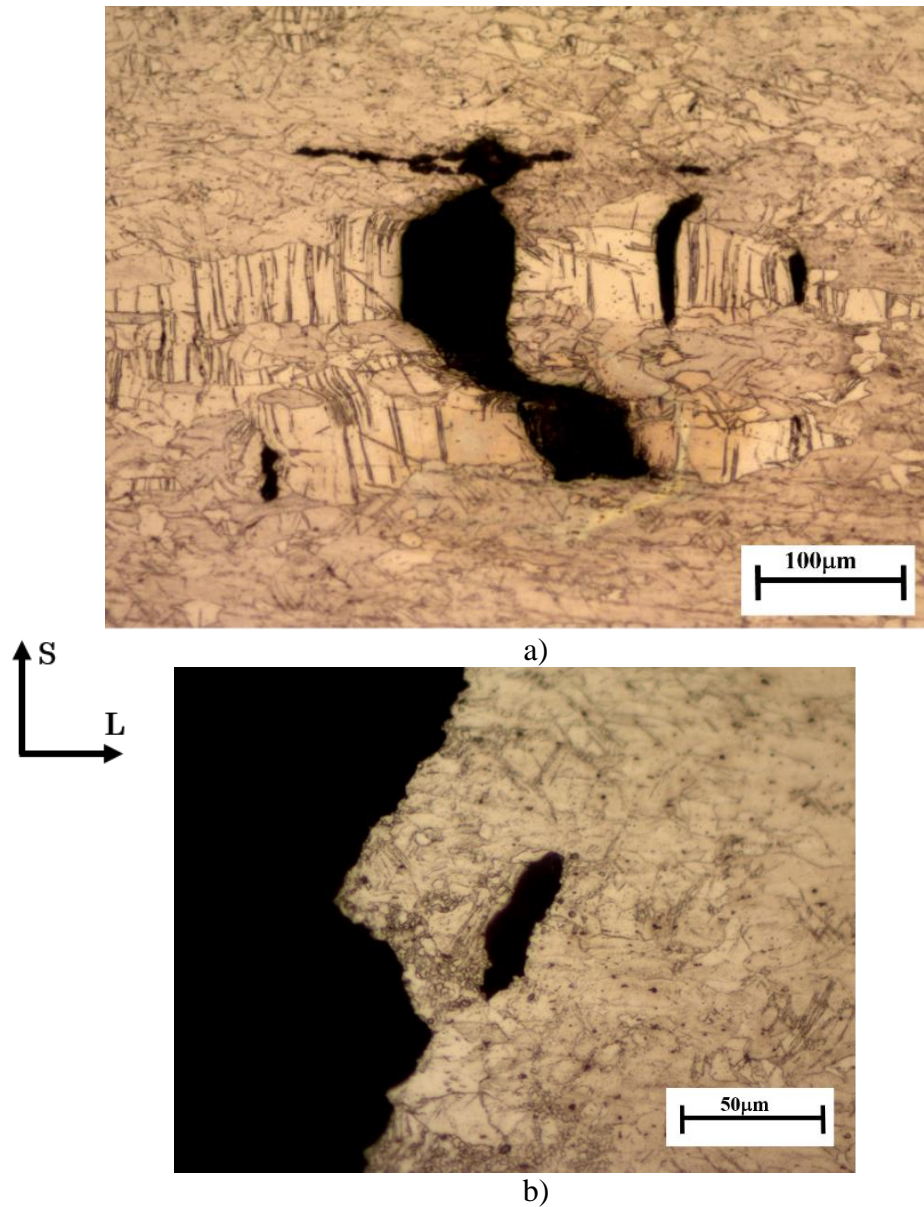


**Figure 3.17** OM micrograph of post-mortem specimen tested at  $10^{-3} \text{ s}^{-1}$ : a) Detail of coalescence of twin-related and second phase particle nucleated voids. b) Micro crack near fracture surface.

The post-mortem specimen corresponding to  $10^{-1} \text{ s}^{-1}$  is shown in figure 3.18. It is noted that there is significant difference in number and size of micro-voids and cracks compared to the specimen interrupted at strain to failure initiation (figure 3.18a). Figure 3.18b shows the typical micro-crack type observed in samples deformed at  $10^{-1} \text{ s}^{-1}$ , similar to the ones found in the interrupted test specimens, with micro-voids elongated along the loading direction L. The post-mortem specimen, however, does exhibit one instance of a twin-related crack, as seen in figure 3.18c. This crack was the only void related to twinning that was present in the specimen. Similarly to the post-mortem  $10^{-3} \text{ s}^{-1}$  specimen, at  $10^{-1} \text{ s}^{-1}$  some cracks parallel to the fracture surface (Figure 3.18d) suggest failure by shear localization.

In order to study the effect of temperature on damage, figure 3.19 shows details of damage on the LS plane of an interrupted test specimen at  $10^{-1} \text{ s}^{-1}$  and  $200^\circ\text{C}$ . The surface of the LS plane exhibit similar type, size and number of micro-cracks to the LS plane of the specimen tested at  $100^\circ\text{C}$ . However, study of the LS plane in the mid-section of the specimen at  $200^\circ\text{C}$  revealed the coexistence of numerous twin-related micro-cracks with second-phase nucleated micro cracks. Together with the effect of strain rate, the results of the effect of temperature seems to show that the conditions that lead to lower twinning density usually develops more twin-nucleated voids. An observation made across all the specimens with twin-sized cracks was that the cracks seemed to form exclusively in the largest twinned grains instead of smaller twinned grains.

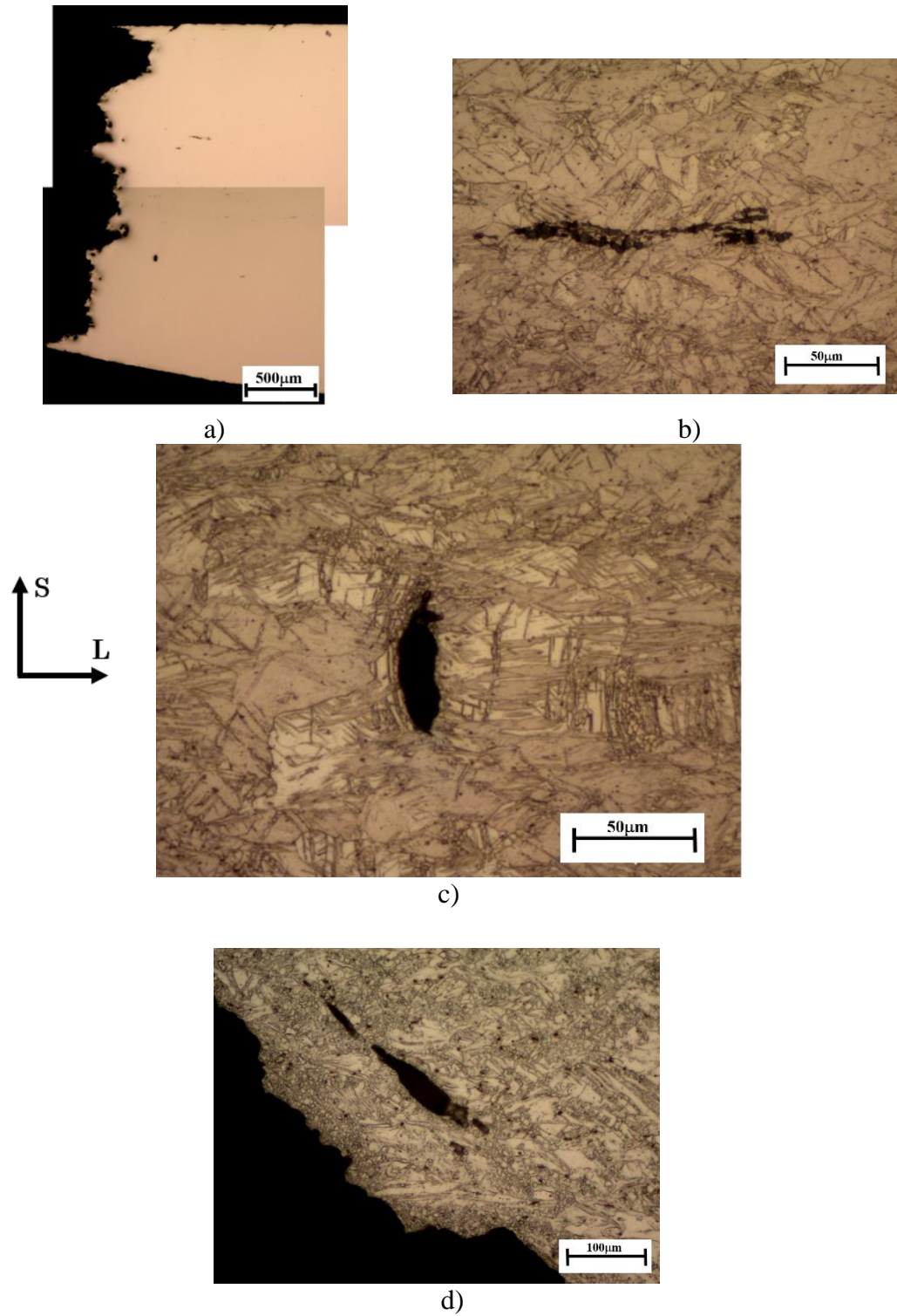
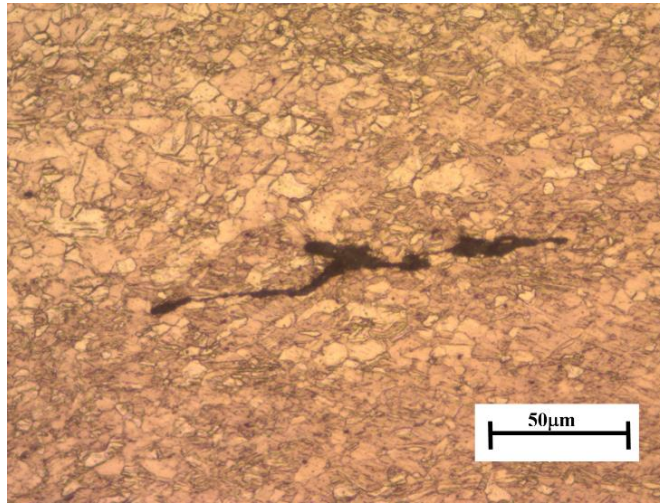
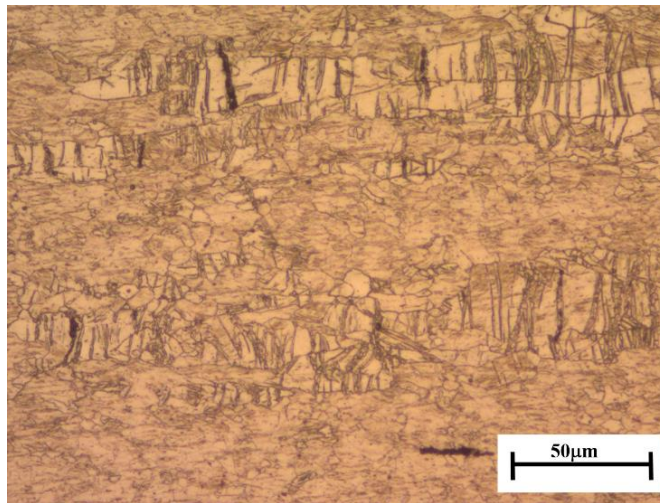
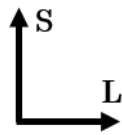


**Figure 3.18** OM micrograph of post-mortem specimen tested at  $10^{-1} \text{ s}^{-1}$ : a) Detail of necklace type micro voids. b) The only instance of twin-related micro-crack found in a  $10^{-1} \text{ s}^{-1}$  and  $100^\circ\text{C}$  specimen.



a)



b)

**Figure 3.19** OM micrograph of uniaxial tensile specimen tested interrupted at strain before failure at  $10^{-1} \text{ s}^{-1}$  and  $200^\circ\text{C}$  showing: a) second-phase nucleated micro-cracks on the specimen surface and, b) micro cracks elongated along twin bands found exclusively in the mid-section of the specimen.

In this study, three main observations have emerged from our experiments on the effect of strain rate and temperature on the damage mechanisms in AZ31 Mg alloy: i) samples tested at lower strain rate and higher temperature exhibited a higher amount of damage (qualitatively estimated by direct observation of number and size of micro-voids and cracks); ii) nucleation at second phase particles is active under all the conditions studied; and iii) on samples tested at highest strain rate and lowest temperature, fewer twinning related cracks were observed. Two different processes could be responsible for the formation of twin sized cracks:

- i) Plastic strain accumulation in twins or decohesion at the twin boundaries: the crystals within the double twins formed during deformation are more prone to basal slip, as a result of the crystal reorientation induced by double twinning. This higher basal slip activity leads to localized shear that will eventually lead to crack formation [76], 75].
- ii) Cracks are formed first, and then twinning is induced by the stress concentration at the tip region of the cracks. In turn, the boundaries of the newly formed twin promote nucleation of new cracks, suggesting a cyclic process of crack and twinning formation[32].

However, the most interesting finding is the correlation between strain rate, temperature and the frequency of twin-sized cracks. Although it is known that higher strain rates and lower temperatures promote contraction and  $\{10\bar{1}1\}$ - $\{10\bar{1}2\}$  double twinning (figure 3.17), very few twin-related cracks are observed under these circumstances. Yoo [77] reported and discussed the competition between twin nucleation and cleavage crack

formation during deformation of magnesium, based on the critical stresses needed for each phenomena to occur. An argument analogous to Yoo's, based on a competition between the minimum stresses required for twinning and twin-cracks formation cannot be directly established in this study, since the conditions with highest twinning density and lowest frequency of twin-sized cracks also correspond to highest stress levels achieved. The observed trends, i.e., the larger number of twin nucleated cracks at the lowest strain rate ( $10^{-3} \text{ s}^{-1}$ ) and the highest temperature ( $200^\circ\text{C}$ ) studied, contrast with the fact that at lower strain rates and higher temperatures reduce twinning density by promoting the activation of other deformation mechanisms.

Moreover, high strain rates and low temperatures promote grain incoherence, and so, it would be expected that the interface stresses between matrix and twinned grains would be highest and thus crack formation at twin boundaries would be favored compared to the lower strain rates and high temperature counterpart.

Based on this analysis, a couple of hypothesis can be proposed that relates the crack-formation at twin boundaries with rate effects, internal stress distribution and grain size effects. Firstly, and though twinning process itself is not rate dependent or thermally activated, we could think of the crack formation at twin boundaries as a rate dependent mechanism. This might imply control of the cracking process by diffusion mechanisms; as well as the effect of the evolution of grain size on twinning. If the nucleation of cracks at twin boundaries is mediated by diffusion processes, then, despite the higher twinning volume fraction at  $10^{-1} \text{ s}^{-1}$  and  $100^\circ\text{C}$ , the material deformed at  $10^{-3} \text{ s}^{-1}$   $100^\circ\text{C}$  and  $10^{-1} \text{ s}^{-1}$   $200^\circ\text{C}$  provides more favorable conditions for the formation of cracks in twinned

regions. Moreover, complex evolution of the grain size, orientation and redistribution of stresses during the nucleation and growth of twinning might also account for the observed trends. Dynamic recrystallization can also play an important role in providing the proper conditions for crack nucleation at twin boundaries by affecting grain size and mis-orientation of newly created grains. A “shielding” effect might occur at high strain rates and low temperatures where long range interactions of twinning might results in internal strains lower than the matrix stresses. Therefore, reaching the critical stresses for crack formation at twinned regions becomes more difficult.

Further studies are necessary in order to address this questions. Efforts are being made in order to understand the internal strain and stresses at twinned regions [78-81]. However, these studies focus mostly on extension twinning; the evolution of strain compatibility in contraction and double twinning needs further investigation. Further experimental test including loading and unloading experiment with the corresponding microstructural examination could be valuable in order to elucidate the phenomena observed.

Our findings regarding damage initiation mechanisms indicate that the crack nucleation sites in magnesium alloys are affected by temperature and strain rate and could be correlated to the macroscopic fracture behavior of magnesium. Moreover, the microscopic observations are in correlation with the evolutions of  $W_f$ : i) at  $10^{-3} \text{ s}^{-1}$ , the formation of a considerable number of voids and cracks helps dissipating more energy than the counterpart at  $10^{-1} \text{ s}^{-1}$ ; while ii) at  $200^\circ\text{C}$ , the slight increase in micro-voids at twin sites could justify the slight increase in  $W_f$  at  $10^{-1} \text{ s}^{-1}$ .

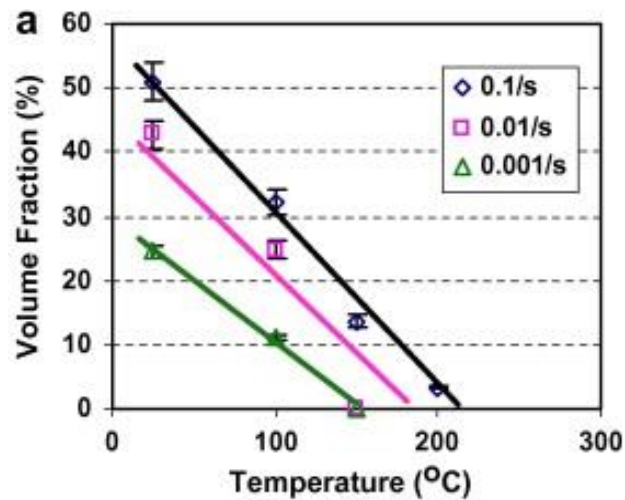


**Figure 3.20** The dependence of volume fractions of contraction and double twins on strain rate in the AZ31, reprinted with permission from [62].

### 3.4 Conclusion

This study investigated the effect of temperature and strain rate on the fracture and damage of AZ31B magnesium alloy sheets. From the results obtained, the following conclusions can be drawn:

1. The fracture behavior of the AZ31 magnesium alloy plates was described in terms of work to fracture  $W_f$ .  $W_f$  evolution with strain rate exhibited a maximum at a strain rate that depends on temperature. Conversely, at a fixed strain rate  $W_f$  exhibits a maximum with temperature.
2. The effect of strain rate and temperature on  $W_f$  is a combination of: i) SRS of the strain to failure, flow stress, ii) thermal softening and; iii) complex rate

and temperature effects on the damage process: difference in the ability to sustain damage.

3. Twinning and second phase particles are identified as the preferred nucleation sites for damage in the specimens studied.
4. Second phase particles were active as damage nucleation sites across all the conditions and planes studied:  $10^{-3} \text{ s}^{-1}$  at  $100^\circ\text{C}$ ,  $10^{-1} \text{ s}^{-1}$  at  $100^\circ\text{C}$  and  $10^{-1} \text{ s}^{-1}$  at  $200^\circ\text{C}$ . The cracks associated to second phase particles elongated along the loading direction.
5. The frequency of twin-sized cracks was highest under conditions where the twinning density was lowest, i.e. at  $10^{-3} \text{ s}^{-1}$  at  $100^\circ\text{C}$  (lowest strain rate studied) and  $10^{-1} \text{ s}^{-1}$  at  $200^\circ\text{C}$  (higher temperature studied). Some hypothesis were proposed in order to explain this correlation between strain rate, temperature and the twin-sized cracks, which include: i) formation of twin sized cracks is a rate dependent process; ii) shielding effect due to long range interaction of twinning; iii) grain size evolution, DRX and stress redistribution during deformation.
6. The evolution of  $W_f$  is in good agreement with the findings in microstructural damage: i) at  $100^\circ\text{C}$ , at the formation of a larger number of voids and cracks at  $10^{-3} \text{ s}^{-1}$  helps dissipating more energy than its counterpart at  $10^{-1} \text{ s}^{-1}$ ; ii) at  $10^{-1} \text{ s}^{-1}$ , the slight increase in micro-voids at twin sites observed at  $200^\circ\text{C}$ , could justify the slight increase in  $W_f$  relative to its counterpart at  $100^\circ\text{C}$ .

## CHAPTER IV

### CONCLUSIONS

The main goal of this thesis was to study the effect of strain rate and temperature on the fracture and damage of a TRC AZ31B magnesium alloy. Specifically, the research presented tries to address some gaps in the fundamental understanding of the behavior of wrought magnesium: evolution of fracture as described by the work of fracture ( $W_f$ ) and the evolution of damage with strain rate and temperature.

Based on the results obtained, the main conclusions can be summarized as follows:

1. TRC AZ31B magnesium alloy plates have a basal orientation. It has a positive strain rate sensitivity that increases with temperature and it exhibits thermal softening. At 300°C, the strain rate has a major influence on the mechanical behavior of AZ31B. Decreasing the strain rate from  $10^{-1}$  to  $10^{-4}$  s<sup>-1</sup> results in a decrease of the maximum strength of 79% and increases the elongation to fracture in 78%.
2. The evolution of the grain morphology with strain rate and temperature shows higher twinning density as strain rate increases and temperature decreases. The material undergoes dynamic recrystallization (DRX) at 300°C and at strain rates  $\leq 10^{-3}$  s<sup>-1</sup>. The grain size of the alloy decreases with strain at a given strain rate and temperature.

3. The TRC plates show deformation anisotropy under uniaxial tensile loading. This anisotropy, associated with the basal orientation of the plates, varies with temperature and strain rate, as different deformation mechanisms are promoted under various loading conditions.
4. The effect of strain rate and temperature on the work of fracture ( $W_f$ ) is a combination of: i) the strain rate sensibility of the strain to failure and flow stress, ii) thermal softening and; iii) complex rate and temperature effects on the damage process, induced by the difference in the ability of the material to sustain damage under various loading conditions.
5. The findings in microstructural damage correlate with the evolution of  $W_f$ : i) at 100°C, at, larger number of voids and cracks found at  $10^{-3} \text{ s}^{-1}$  helps dissipating more energy than its counterpart at  $10^{-1} \text{ s}^{-1}$ ; ii) at  $10^{-1} \text{ s}^{-1}$ , the slight increase in number of micro-voids at 200°C could justify the slight increase in  $W_f$  relative to its counterpart at 100°C.
6. Second phase particles and twin-sized cracks are identified as the main sites for damage nucleation under the conditions studied. Nucleation at second phase particles was present across all the conditions analyzed. The most interesting finding was the correlation between strain rate, temperature and the frequency of twin-sized cracks was found: the highest frequency of twin-sized cracks is found under the strain rate and temperature that results in the lowest twinning density. Some hypothesis are proposed in order to explain this behavior: i) formation of twin-related cracks is a rate dependent

mechanism, and; ii) shielding effect due to high twinning density decreases the effective stress inside twinned regions. Future work in order to validate any of these hypothesis includes loading/unloading experiments under at the same conditions evaluated ( $10^{-3}$  and  $10^{-1} \text{ s}^{-1}$  at  $100^\circ\text{C}$ ,  $10^{-1} \text{ s}^{-1}$  at  $200^\circ\text{C}$ ). Further investigations can evaluate the same conditions here studied through electron backscatter diffraction (EBSD) in order to obtain information regarding changes in orientation after deformation, with special interest in the evolution of orientation in both twinned zones with micro-cracks and intact twinned zones.

## REFERENCES

1. Aghion, E., B. Bronfin, and D. Eliezer, *The role of the magnesium industry in protecting the environment*. Journal of Materials Processing Technology, 2001. 117(3): p. 381-385.
2. Hakamada, M., T. Furuta, Y. Chino, Y. Chen, H. Kusuda, et al., *Life cycle inventory study on magnesium alloy substitution in vehicles*. Energy, 2007. 32(8): p. 1352-1360.
3. Robson, J.D., *Critical assessment: Wrought magnesium alloys*. Materials Science and Technology, 2014. 31(3): p. 257-264
4. Luo, A.A. and A.K. Sachdev, *12 - Applications of magnesium alloys in automotive engineering*, in *Advances in wrought magnesium alloys*, C. Bettles and M. Barnett, Editors. 2012, Woodhead Publishing: Cambridge, United Kingdom. p. 393-426.
5. Powell, B.R., P.E. Krajewski, and A.A. Luo, *4 - Magnesium alloys for lightweight powertrains and automotive structures*, in *Materials, design and manufacturing for lightweight vehicles*, P.K. Mallick, Editor. 2010, Woodhead Publishing: Cambridge, United Kingdom. p. 114-173.
6. Essadiqi, E., I.H. Jung, and M.A. Wells, *7 - Twin roll casting of magnesium*, in *Advances in wrought magnesium alloys*, C. Bettles and M. Barnett, Editors. 2012, Woodhead Publishing: Cambridge, United Kingdom. p. 272-303.

7. Dogan, E., I. Karaman, G. Ayoub, and G. Kridli, *Reduction in tension–compression asymmetry via grain refinement and texture design in Mg–3Al–1Zn sheets*. Materials Science and Engineering: A, 2014. 610(0): p. 220-227.
8. Watari, H., T. Haga, N. Koga, and K. Davey, *Feasibility study of twin roll casting process for magnesium alloys*. Journal of Materials Processing Technology, 2007. 192–193(0): p. 300-305.
9. Agnew, S.R., 2 - *Deformation mechanisms of magnesium alloys*, in *Advances in wrought magnesium alloys*, C. Bettles and M. Barnett, Editors. 2012, Woodhead Publishing: Cambridge, United Kingdom. p. 63-104.
10. Agnew, S.R. and Ö. Duygulu, *Plastic anisotropy and the role of non-basal slip in magnesium alloy AZ31B*. International Journal of Plasticity, 2005. 21(6): p. 1161-1193.
11. Koike, J., T. Kobayashi, T. Mukai, H. Watanabe, M. Suzuki, et al., *The activity of non-basal slip systems and dynamic recovery at room temperature in fine-grained AZ31B magnesium alloys*. Acta Materialia, 2003. 51(7): p. 2055-2065.
12. Barnett, M.R., *Twinning and the ductility of magnesium alloys: Part I: “Tension” twins*. Materials Science and Engineering: A, 2007. 464(1–2): p. 1-7.
13. Reed-Hill, R. and W. Robertson, *The crystallographic characteristics of fracture in magnesium single crystals*. Acta Metallurgica, 1957. 5(12): p. 728-737.
14. Barnett, M.R., 3 - *Twinning and its role in wrought magnesium alloys*, in *Advances in wrought magnesium alloys*, C. Bettles and M. Barnett, Editors. 2012, Woodhead Publishing: Cambridge, United Kingdom. p. 105-143.

15. Barnett, M.R., *Twinning and the ductility of magnesium alloys: Part II. "Contraction" twins*. Materials Science and Engineering: A, 2007. 464(1–2): p. 8-16.
16. Keshavarz, Z. and M.R. Barnett, *EBSD analysis of deformation modes in Mg–3Al–1Zn*. Scripta Materialia, 2006. 55(10): p. 915-918.
17. Mayama, T., M. Noda, R. Chiba, and M. Kuroda, *Crystal plasticity analysis of texture development in magnesium alloy during extrusion*. International Journal of Plasticity, 2011. 27(12): p. 1916-1935.
18. Kondori, B. and A.A. Benzerga, *Effect of stress triaxiality on the flow and fracture of Mg alloy AZ31*. Metallurgical and Materials Transactions A, 2014. 45(8): p. 3292-3307.
19. Zhang, Z., P. Cizek, and M. Barnett, *A critical test of twin-induced softening in a magnesium alloy extruded to a strain of 0.7 at room temperature*. Scripta Materialia, 2012. 67(12): p. 1015-1018.
20. Laser, T., M.R. Nürnberg, A. Janz, C. Hartig, D. Letzig, et al., *The influence of manganese on the microstructure and mechanical properties of AZ31 gravity die cast alloys*. Acta Materialia, 2006. 54(11): p. 3033-3041.
21. Lugo, M., M.A. Tschopp, J.B. Jordon, and M.F. Horstemeyer, *Microstructure and damage evolution during tensile loading in a wrought magnesium alloy*. Scripta Materialia, 2011. 64(9): p. 912-915.

22. Stanford, N. and D. Atwell, *The effect of Mn-rich precipitates on the strength of AZ31 extrudates*. Metallurgical and Materials Transactions A, 2013. 44(10): p. 4830-4843.
23. Hort, N., Y. Huang, and K.U. Kainer, *Intermetallics in magnesium alloys*. Advanced Engineering Materials, 2006. 8(4): p. 235-240.
24. Kondori, B. and A.A. Benzerga, *Fracture strains, damage mechanisms and anisotropy in a magnesium alloy across a range of stress triaxialities*. Experimental Mechanics, 2014. 54(3): p. 493-499.
25. Marya, M., L.G. Hector, R. Verma, and W. Tong, *Microstructural effects of AZ31 magnesium alloy on its tensile deformation and failure behaviors*. Materials science and engineering: A, 2006. 418(1): p. 341-356.
26. Al-Samman, T. and G. Gottstein, *Room temperature formability of a magnesium AZ31 alloy: Examining the role of texture on the deformation mechanisms*. Materials Science and Engineering: A, 2008. 488(1-2): p. 406-414.
27. Ando, D., J. Koike, and Y. Sutou, *Relationship between deformation twinning and surface step formation in AZ31 magnesium alloys*. Acta Materialia, 2010. 58(13): p. 4316-4324.
28. Ando, D., J. Koike, and Y. Sutou, *The role of deformation twinning in the fracture behavior and mechanism of basal textured magnesium alloys*. Materials Science and Engineering: A, 2014. 600(0): p. 145-152.

29. Kelley, E. and W. Hosford, *Plane-strain compression of magnesium and magnesium alloy crystals*. Transactions of the Metallurgical Society of AIME, 1968. 242(1): p. 5-13.
30. Yoshinaga, H., T. Obara, and S. Morozumi, *Twinning deformation in magnesium compressed along the c-axis*. Materials Science and Engineering, 1973. 12(5–6): p. 255-264.
31. Ando, D., J. Koike, and Y. Sutou, *The role of deformation twinning in the fracture behavior and mechanism of basal textured magnesium alloys*. Materials Science and Engineering: A, 2014. 600: p. 145-152.
32. Lu, L., T. Liu, Y. Chen, and Z. Wang, *Deformation and fracture behavior of hot extruded Mg alloys AZ31*. Materials Characterization, 2012. 67(0): p. 93-100.
33. Peng, W.P., P.J. Li, P. Zeng, and L.P. Lei, *Hot deformation behavior and microstructure evolution of twin-roll-cast Mg–2.9Al–0.9Zn alloy: A study with processing map*. Materials Science and Engineering: A, 2008. 494(1–2): p. 173-178.
34. Yin, D.L., K.F. Zhang, G.F. Wang, and W.B. Han, *Warm deformation behavior of hot-rolled AZ31 Mg alloy*. Materials Science and Engineering: A, 2005. 392(1): p. 320-325.
35. Nakaura, Y., A. Watanabe, and K. Ohori, *Microstructure and mechanical properties of AZ31 magnesium alloy strip produced by twin roll casting*. Materials Transactions, 2006. 47(7): p. 1743-1749.

36. Cheng, Y., Z. Chen, W. Xia, and T. Zhou, *Improvement of drawability at room temperature in AZ31 magnesium alloy sheets processed by equal channel angular rolling*. Journal of Materials Engineering and Performance, 2008. 17(1): p. 15-19.
37. Essadiqi, E., *Magnesium sheet technology perspectives*. The Journal of The Minerals, Metals & Materials Society, 2009. 61(8): p. 13-13.
38. Zarandi, F., G. Seale, R. Verma, E. Essadiqi, and S. Yue, *Effect of Al and Mn additions on rolling and deformation behavior of AZ series magnesium alloys*. Materials Science and Engineering: A, 2008. 496(1-2): p. 159-168.
39. Cook, R., P.G. Grocock, P.M. Thomas, D.V. Edmonds, and J.D. Hunt, *Development of the twin-roll casting process*. Journal of Materials Processing Technology, 1995. 55(2): p. 76-84.
40. Watari, H., K. Davey, M.T. Rasgado, T. Haga, and S. Izawa, *Semi-solid manufacturing process of magnesium alloys by twin-roll casting*. Journal of Materials Processing Technology, 2004. 155-156(0): p. 1662-1667.
41. Boileau, J.M., P.A. Friedman, D.Q. Houston, and S.G. Luckey, *Superplastic response of continuously cast AZ31B magnesium sheet alloys*. Journal of Materials Engineering and Performance, 2010. 19(4): p. 467-480.
42. Chen, X.-p., D. Shang, R. Xiao, G.-j. Huang, and Q. Liu, *Influence of rolling ways on microstructure and anisotropy of AZ31 alloy sheet*. Transactions of Nonferrous Metals Society of China, 2010. 20, Supplement 2(0): p. s589-s593.

43. Kaya, A.A., O. Duygulu, S. Ucuncuoglu, G. Oktay, D.S. Temur, et al., *Production of 150 cm wide AZ31 magnesium sheet by twin roll casting*. Transactions of Nonferrous Metals Society of China, 2008. 18, Supplement 1(0): p. s185-s188.
44. Liang, D. and C.B. Cowley, *The twin-roll strip casting of magnesium*. The Journal of The Minerals, Metals & Materials Society, 2004. 56(5): p. 26-28.
45. Masoumi, M., F. Zarandi, and M. Pekguleryuz, *Microstructure and texture studies on twin-roll cast AZ31 (Mg-3wt.%Al-1wt.%Zn) alloy and the effect of thermomechanical processing*. Materials Science and Engineering: A, 2011. 528(3): p. 1268-1279.
46. Zi, A. and H. Palkowski, *Direct strip casting and hot rolling of an AZ31 magnesium alloy*. Materials Science and Engineering: A, 2010. 528(2): p. 559-565.
47. You, B.S., C.D. Yim, and S.H. Kim, *Solidification of AZ31 magnesium alloy plate in a horizontal continuous casting process*. Materials Science and Engineering: A, 2005. 413: p. 139-143.
48. Lee, B.H., S.H. Park, S.-G. Hong, K.-T. Park, and C.S. Lee, *Role of initial texture on the plastic anisotropy of Mg-3Al-1Zn alloy at various temperatures*. Materials Science and Engineering: A, 2011. 528(3): p. 1162-1172.
49. Abu-Farha, F.K. and M.K. Khraisheh, *Analysis of superplastic deformation of AZ31 magnesium alloy*. Advanced Engineering Materials, 2007. 9(9): p. 777-783.

50. Abu-Farha, F.K. and M.K. Khraisheh, *Post-superplastic forming analysis under different loading paths. Part one: Uniaxial loading case*. Journal of Materials Engineering and Performance, 2008. 17(2): p. 153-162.
51. Chino, Y., K. Kimura, and M. Mabuchi, *Twinning behavior and deformation mechanisms of extruded AZ31 mg alloy*. Materials Science and Engineering: A, 2008. 486(1–2): p. 481-488.
52. Koike, J., R. Ohyama, T. Kobayashi, M. Suzuki, and K. Maruyama, *Grain-boundary sliding in AZ31 magnesium alloys at room temperature to 523 K*. Materials Transactions, 2003. 44(4): p. 445-451.
53. Wang, Y.N. and J.C. Huang, *The role of twinning and untwinning in yielding behavior in hot-extruded Mg–Al–Zn alloy*. Acta Materialia, 2007. 55(3): p. 897-905.
54. Al-Samman, T. and G. Gottstein, *Dynamic recrystallization during high temperature deformation of magnesium*. Materials Science and Engineering: A, 2008. 490(1): p. 411-420.
55. Welsch, G., R. Boyer, and E. Collings, *Materials properties handbook: Titanium alloys*. 1993. ASM international: Materials Park, OH. p. 1101-1103.
56. Maksoud, I.A., H. Ahmed, and J. Rödel, *Investigation of the effect of strain rate and temperature on the deformability and microstructure evolution of AZ31 magnesium alloy*. Materials Science and Engineering: A, 2009. 504(1–2): p. 40-48.

57. Vagarali, S.S. and T.G. Langdon, *Deformation mechanisms in H.C.P. metals at elevated temperatures—I. Creep behavior of magnesium*. Acta Metallurgica, 1981. 29(12): p. 1969-1982.
58. Frost, H.J. and F. Ashby, *Deformation-mechanism maps: The plasticity and creep of metals and ceramics*. 1982. Pergamon Press: Oxford, United Kingdom.
59. Jiang, L., J.J. Jonas, A.A. Luo, A.K. Sachdev, and S. Godet, *Twinning-induced softening in polycrystalline AM30 Mg alloy at moderate temperatures*. Scripta Materialia, 2006. 54(5): p. 771-775.
60. Yi, S., S. Zaefferer, and H.-G. Brokmeier, *Mechanical behaviour and microstructural evolution of magnesium alloy AZ31 in tension at different temperatures*. Materials Science and Engineering: A, 2006. 424(1): p. 275-281.
61. Doherty, R.D., D.A. Hughes, F.J. Humphreys, J.J. Jonas, D.J. Jensen, et al., *Current issues in recrystallization: A review*. Materials Science and Engineering: A, 1997. 238(2): p. 219-274.
62. Jiang, L., J. Jonas, R. Mishra, A. Luo, A. Sachdev, et al., *Twinning and texture development in two Mg alloys subjected to loading along three different strain paths*. Acta Materialia, 2007. 55(11): p. 3899-3910.
63. Rodriguez, A., G. Kridli, G. Ayoub, and H. Zbib, *Effects of the strain rate and temperature on the microstructural evolution of twin-rolled cast wrought AZ31B alloys sheets*. Journal of Materials Engineering and Performance, 2013. 22(10): p. 3115-3125.

64. Xu, S., W. Tyson, R. Bouchard, and V. Gertsman, *Effects of strain rate and temperature on tensile flow behavior and energy absorption of extruded magnesium AM30 alloy*. Journal of Materials Engineering and Performance, 2009. 18(8): p. 1091-1101.
65. Ahmad, I.R., X. Jing, and D.W. Shu, *Effect of temperature on the mechanical behaviour of magnesium alloy AZ91D in the range between  $-30\text{ }^{\circ}\text{C}$  and  $250\text{ }^{\circ}\text{C}$* . International Journal of Mechanical Sciences, 2014. 86(0): p. 34-45.
66. Penghuai, F., P. Liming, J. Haiyan, Z. Zhenyan, and Z. Chunquan, *Fracture behavior and mechanical properties of Mg-4Y-2Nd-1Gd-0.4Zr (wt.%) alloy at room temperature*. Materials Science and Engineering A, 2008. 486(1-2): p. 572-579.
67. Reed-Hill, R. and W. Robertson, *Additional modes of deformation twinning in magnesium*. Acta Metallurgica, 1957. 5(12): p. 717-727.
68. Reed-Hill, R.E. and W.D. Robertson, *Deformation of magnesium single crystals by nonbasal slip*. Journal of Metals Transactions AIME, 1957. 220: p. 496-502.
69. Kobayashi, Y., T. Shibusawa, and K. Ishikawa. *Environmental effect of fatigue crack propagation of magnesium alloy*. Materials Science and Engineering A, 1997. 234: p. 220-222.
70. Mehrzadi, M. and F. Taheri, *Influence of compressive cyclic loading on crack propagation in AM60B magnesium alloy under random and constant amplitude cyclic loadings*. Engineering Fracture Mechanics, 2013. 99: p. 1-17.

71. Uematsu, Y., T. Kakiuchi, M. Nakajima, Y. Nakamura, S. Miyazaki, et al., *Fatigue crack propagation of AZ61 magnesium alloy under controlled humidity and visualization of hydrogen diffusion along the crack wake*. International Journal of Fatigue, 2014. 59: p. 234-243.
72. Zeng, R., Y. Xu, W. Ke, and E. Han, *Fatigue crack propagation behavior of an as-extruded magnesium alloy AZ80*. Materials Science and Engineering: A, 2009. 509(1): p. 1-7.
73. Kang, J., D.S. Wilkinson, R.K. Mishra, J.D. Embury, E. Essadiqi, et al., *Microstructural aspects of damage and fracture in AZ31 sheet materials*. Journal of materials engineering and performance, 2013. 22(5): p. 1386-1395.
74. Lu, L., T. Liu, Y. Chen, and Z. Wang, *Deformation and fracture behavior of hot extruded Mg alloys AZ31*. Materials Characterization, 2012. 67: p. 93-100.
75. Sarkar, J., T. Kutty, D. Wilkinson, J. Embury, and D. Lloyd, *Tensile properties and bendability of T4 treated AA6111 aluminum alloys*. Materials Science and Engineering: A, 2004. 369(1): p. 258-266.
76. Beyerlein, I.J., J. Wang, M.R. Barnett, and C.N. Tomé, *Double twinning mechanisms in magnesium alloys via dissociation of lattice dislocations*. Proceedings of the Royal Society of London A: Mathematical, Physical and Engineering Sciences. 468(2141): p. 1496-1520.
77. Yoo, M.H., *Slip, twinning, and fracture in hexagonal close-packed metals*. Metallurgical Transactions A, 1981. 12(3): p. 409-418.

78. Aydiner, C., J. Bernier, B. Clausen, U. Lienert, C. Tomé, et al., *Evolution of stress in individual grains and twins in a magnesium alloy aggregate*. Physical Review B, 2009. 80(2): p. 0241131- 0241136.
79. Clausen, B., C.N. Tomé, D.W. Brown, and S.R. Agnew, *Reorientation and stress relaxation due to twinning: Modeling and experimental characterization for Mg*. Acta Materialia, 2008. 56(11): p. 2456-2468.
80. Cizek, P. and M.R. Barnett, *Characteristics of the contraction twins formed close to the fracture surface in Mg–3Al–1Zn alloy deformed in tension*. Scripta Materialia, 2008. 59(9): p. 959-962.
81. Wu, L., S.R. Agnew, D.W. Brown, G.M. Stoica, B. Clausen, et al., *Internal stress relaxation and load redistribution during the twinning–detwinning-dominated cyclic deformation of a wrought magnesium alloy, ZK60A*. Acta Materialia, 2008. 56(14): p. 3699-3707.

## APPENDIX

### A.1 Damage on TS Planes

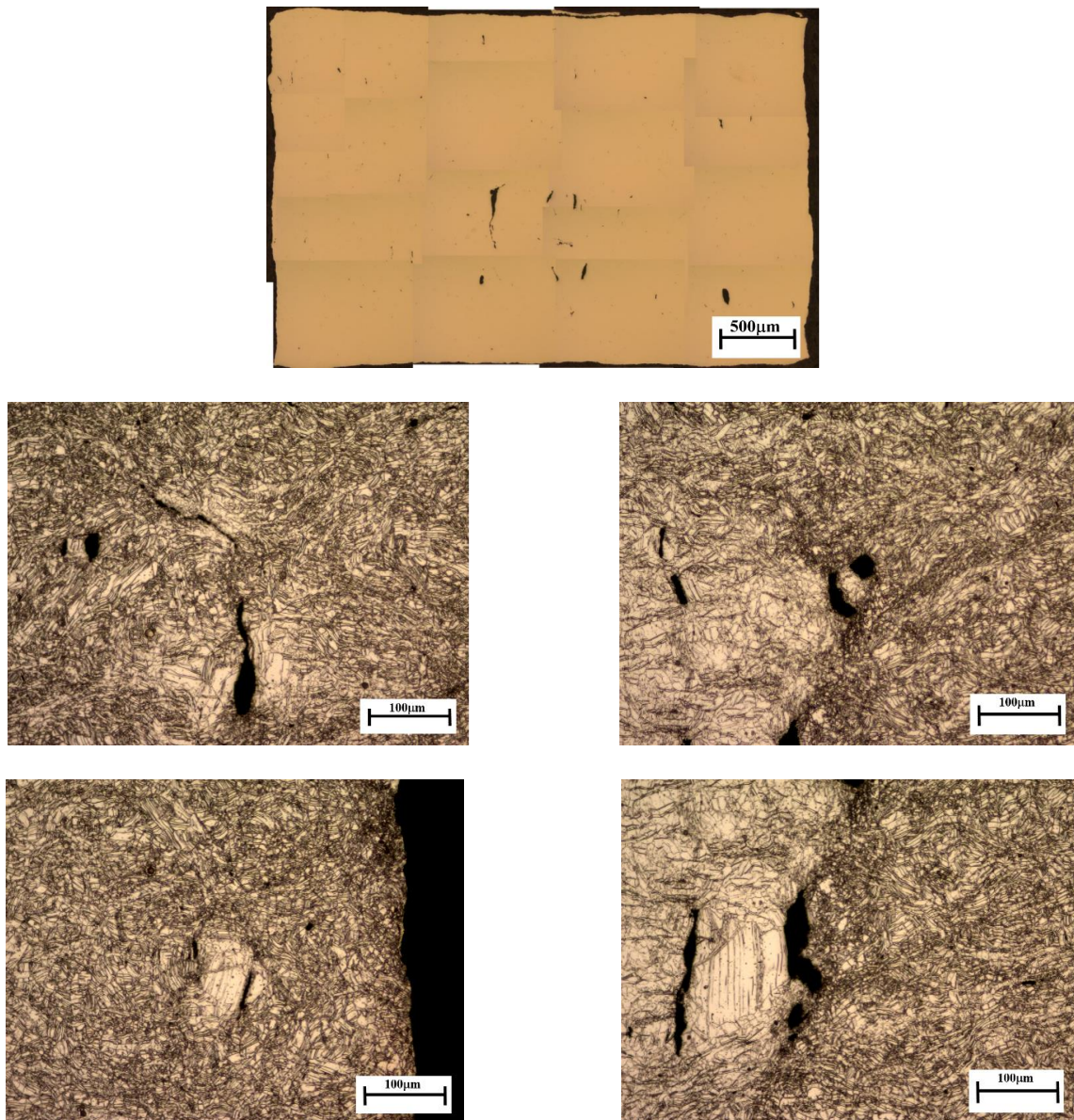


**Figure A.1.1** TS micrographs of TRC AZ31B alloy loaded at  $10^{-3} \text{ s}^{-1}$  and  $100^\circ\text{C}$ .

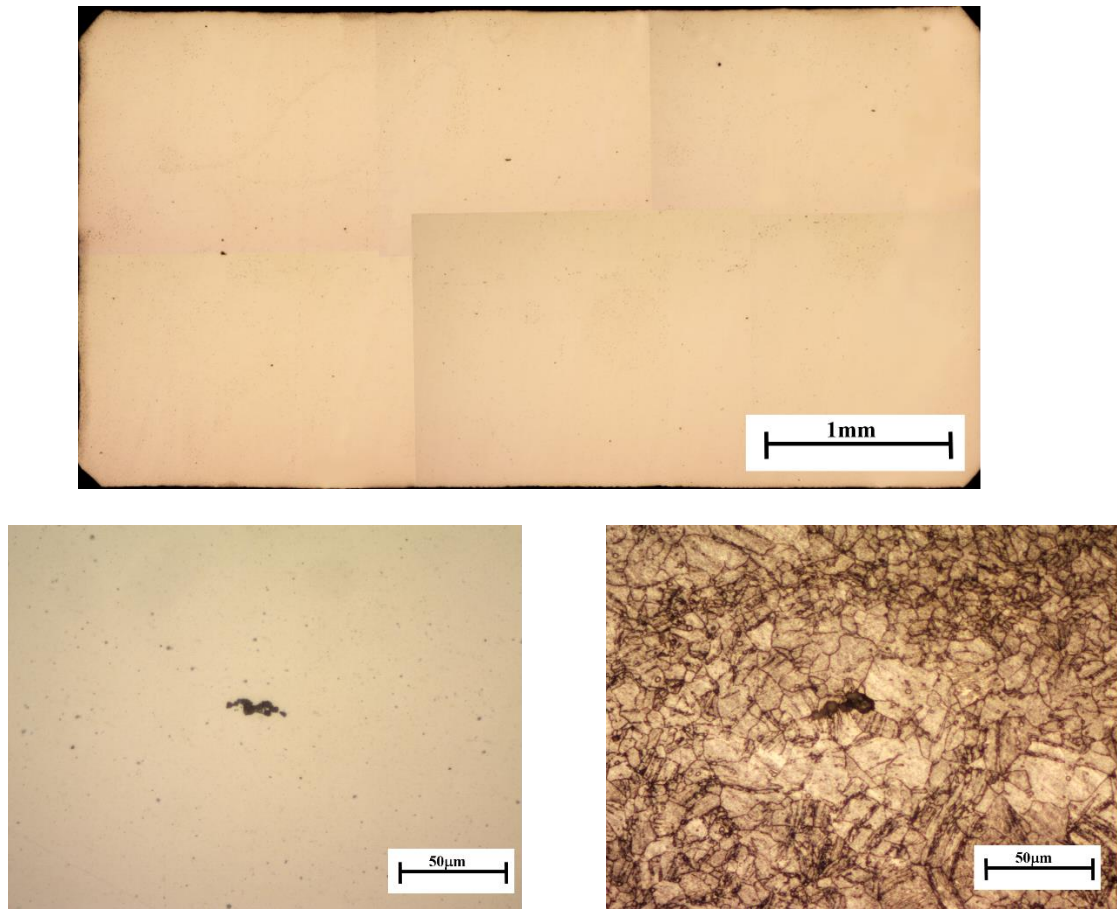


**Figure A.1.2** TS micrographs of TRC AZ31B alloy loaded at  $10^{-1} \text{ s}^{-1}$  and  $100^\circ\text{C}$ .

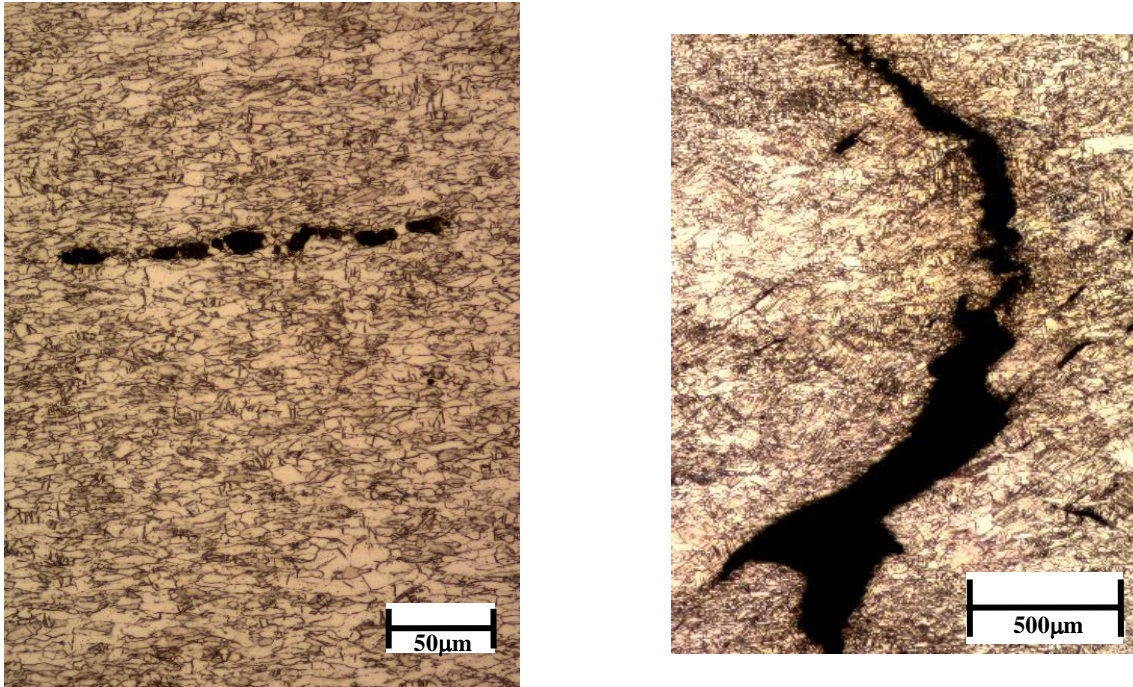


**Figure A.1.3** LT micrographs of TRC AZ31B alloy loaded at  $10^{-3}s^{-1}$  and  $100^{\circ}C$ .

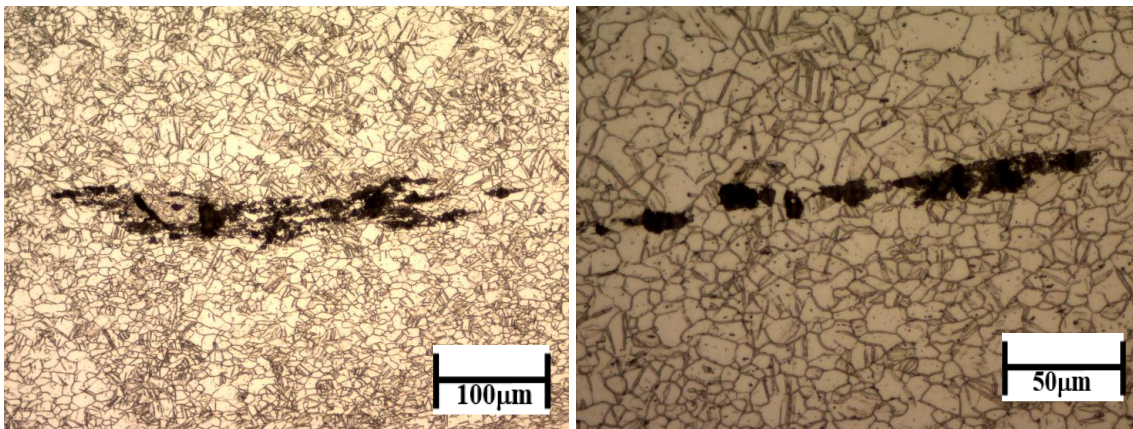


**Figure A.1.4** LT micrographs of TRC AZ31B alloy loaded at  $10^{-1}s^{-1}$  and  $100^{\circ}C$ .

## A.2 Twinning in post-deformed specimen

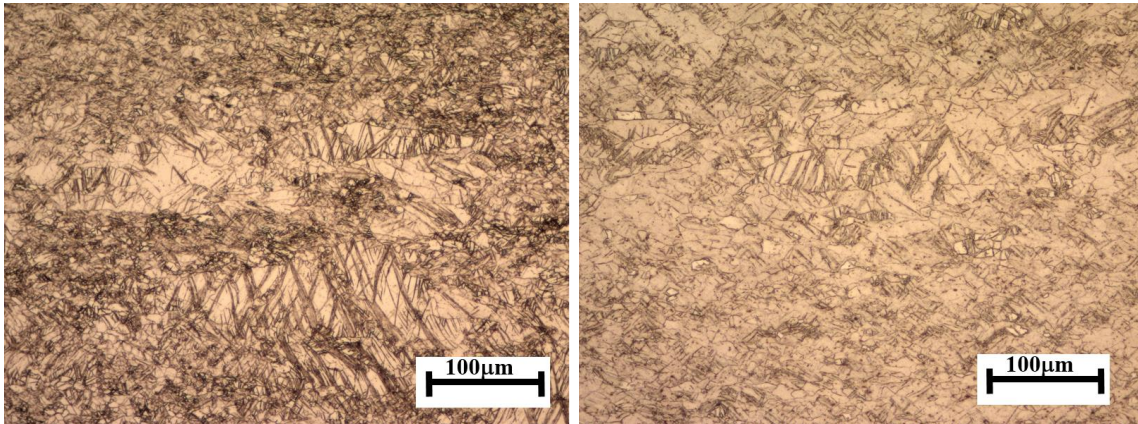


**Figure A.2.1** Twinning found on the LS plane of specimens deformed at  $10^{-1} \text{ s}^{-1}$  and  $100^\circ\text{C}$ .

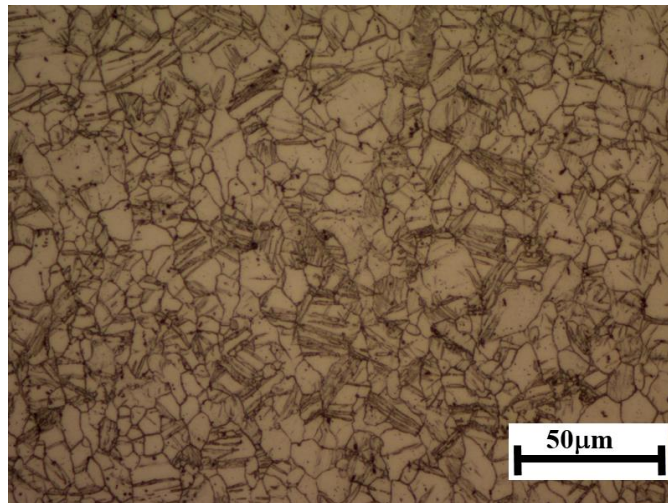


**Figure A.2.2** Twinning found on the LT plane of specimen deformed at  $10^{-2} \text{ s}^{-1}$  and RT.

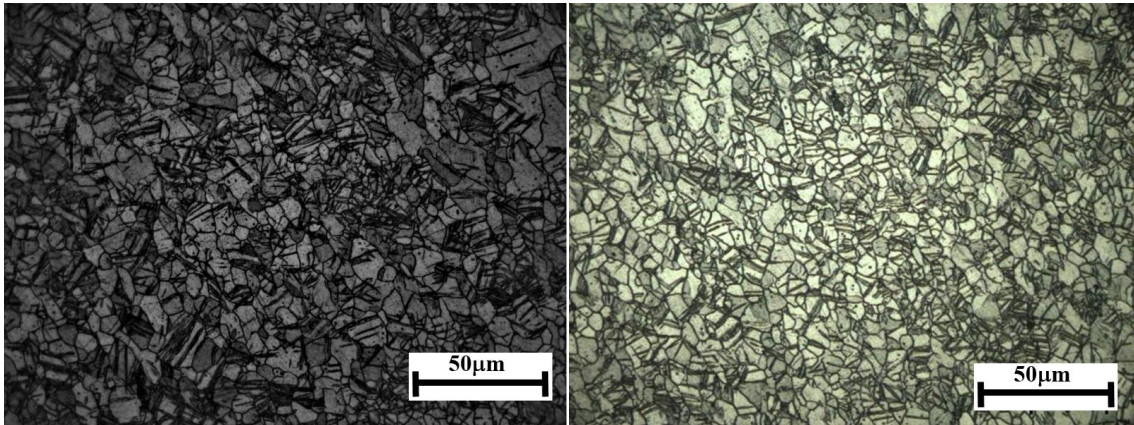


**Figure A.2.3** Twinning found on the LT plane of specimen deformed at  $10^{-3} \text{ s}^{-1}$  and RT.

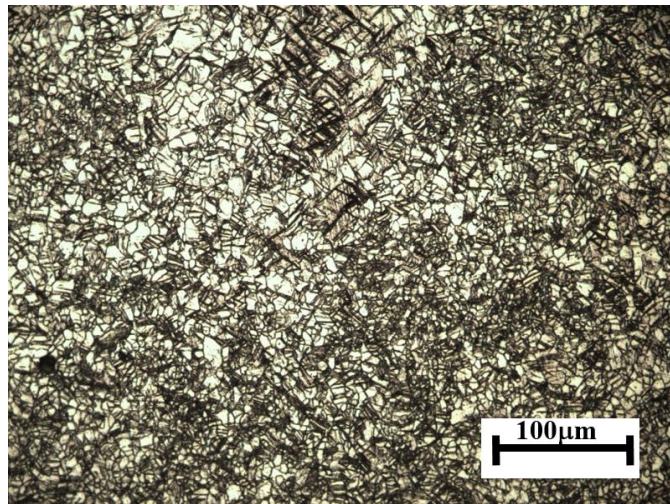


**Figure A.2.4** Twinning found on the LT plane of specimen deformed at  $10^{-1} \text{ s}^{-1}$  and RT.

### A.3 Twin sized voids

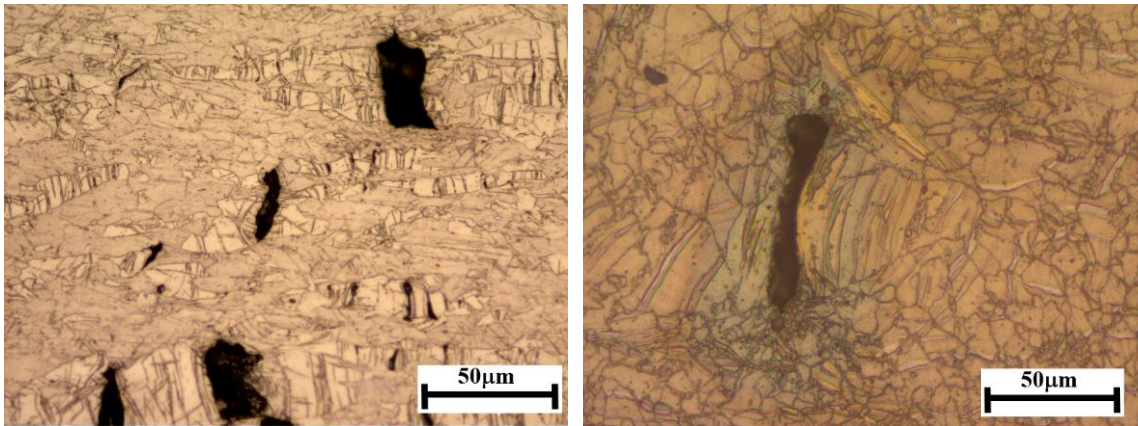


**Figure A.3.1** Twin sized voids found on the LS plane of specimen deformed at  $10^{-1} \text{ s}^{-1}$  and  $200^\circ\text{C}$ .

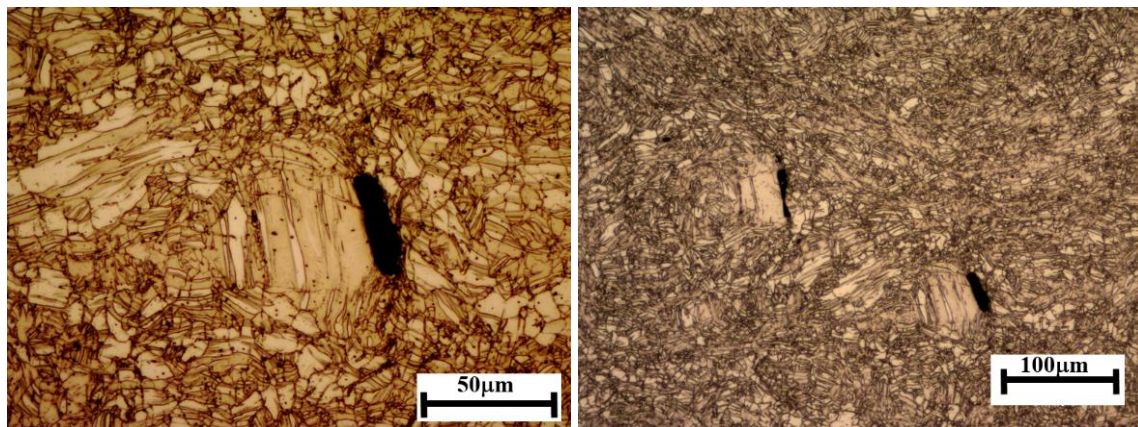


**Figure A.3.2** Twin sized voids found on the TS plane of specimen deformed at  $10^{-3} \text{ s}^{-1}$  and  $100^\circ\text{C}$ .

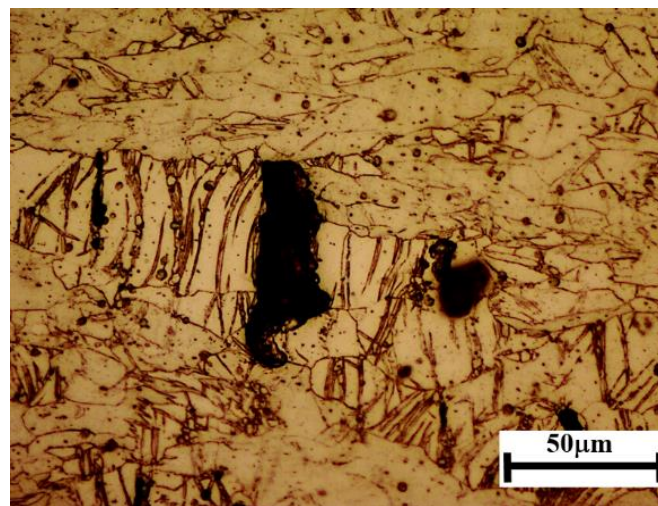
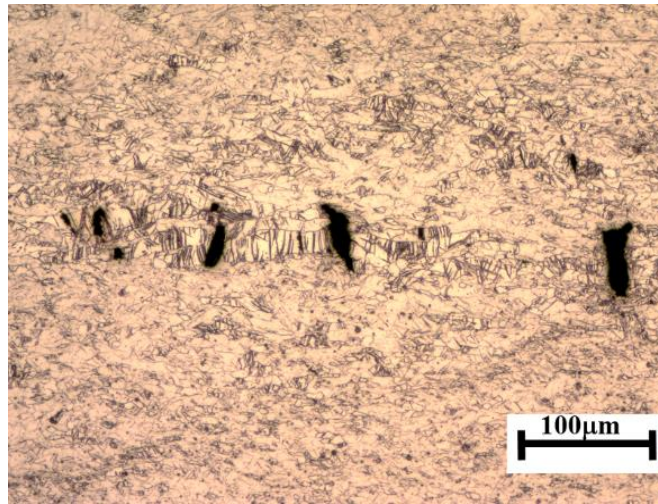


**Figure A.3.3** Twin sized voids found on the LS plane of specimen deformed at  $10^{-3} \text{ s}^{-1}$  and  $100^\circ\text{C}$ .